Electromigration Behavior and Reliability of Bamboo Al(Cu) Interconnects for Integrated Circuits

by

V. T. Srikar

B.Tech., Banaras Hindu University, India (1994)

Submitted to the Department of Materials Science and Engineering in partial fulfillment of the requirements for the degree of

Doctor of Philosophy in Materials Science

at the

MASSACHUSETTS INSTITUTE OF TECHNOLOGY

February 1999

© Massachusetts Institute of Technology 1999. All rights reserved.

Author ....
Department of Materials Science and Engineering
January 8, 1999

Certified by ....
Carl V. Thompson
Stavros Salapatas Professor of Materials Science and Engineering
Thesis Supervisor

Accepted by ....
Linn W. Hobbs
John F. Elliot Professor of Materials
Chairman, Departmental Committee on Graduate Students

Science

Electromigration Behavior and Reliability of Bamboo Al(Cu) Interconnects for Integrated Circuits

by

V. T. Srikar

Submitted to the Department of Materials Science and Engineering
on January 8, 1999, in partial fulfillment of the
requirements for the degree of
Doctor of Philosophy in Materials Science

Abstract

Thin lines of Al(Cu) with bamboo grain structures, capped with Al_3Ti layers and terminating in W-studs, are an increasingly common class of interconnects used in Si integrated circuits. These lines are susceptible to transgranular electromigration-induced failure.

Electromigration-induced stress evolution can be modeled using a diffusion-drift equation in one dimension, the solution of which requires knowledge of the transport parameters. The transgranular diffusion and electromigration characteristics of Al and Cu in Al were unambiguously determined by developing and carrying out experiments using single-crystal Al interconnects fabricated on oxidized Si substrates.

Accelerated electromigration-lifetime tests were conducted on passivated Al single-crystal lines (2.0 μm wide, 0.4 μm thick) capped with polycrystalline Al_3Ti overlayers. The capping layers were formed by the reaction of Al with Ti overlayers. The activation energy for electromigration-induced failure was determined to be 0.94 ± 0.05 eV. Previous work on Al single-crystals without Al_3Ti overlayers resulted in an activation energy of 0.98 ± 0.2 eV, and lifetimes of similar magnitude. It was concluded that the Al_3Ti capping layers do not affect the kinetics and mechanisms of transgranular electromigration. Further, these results suggest that either the rate-limiting mechanism for electromigration-induced failure of single-crystal Al interconnects is not diffusion, or that, surprisingly, the diffusivity of Al along the Al/Al_3Ti interface is approximately equal to, or lower than, the diffusivity of Al along the Al/AlO_x interface.

The diffusion and electromigration characteristics of Cu in single-crystal Al lines were also experimentally studied. Test structures consisted of parallel lines (5.0 μm wide, 0.4 μm thick), with alternating lines terminating in shared contact pads. Copper was locally added to the same regions in all the lines, and the effects of temperature and current-density were characterized by analyzing the concentration-profile of Cu

measured along the length of the lines using electron-probe microanalysis. The activation energy for diffusion was found to be 0.8 ± 0.2 eV in the range 320 - 400 °C, suggesting that the path for diffusion of Cu is along the Al/AlO_x in these single crystals. The apparent effective valence characterizing electromigration (Z^*) was found to be -5.4 ± 1.2 at 350 °C.

Using these results, and employing a previously developed computer program (MIT/EmSim), electromigration-induced stress evolution was simulated in representative bamboo Al and Al(0.2 at% Cu) interconnects, clad with Al_3Ti layers, and terminating in W-studs. The length and current-density were varied in the range 10 - 200 μm and 0.1 - 10 MA/cm^2 respectively, and the temperature (100 °C) was chosen to represent *service* conditions. The critical stresses for nucleation of damage were defined to be 400 MPa in tension, and 800 MPa in compression. Failure maps were constructed using two different failure criteria: an increase in resistance of 25%, and a void length of 1 μm. The initial stress of the line prior to the onset of electromigration was defined to be zero.

The failure maps showed five distinct regions: immortality, resistance saturation, void-nucleation-limited failure, void-growth-limited failure, and dielectric-cracking-limited failure. The choice of the failure criteria was seen to strongly affect the topology of the maps. In addition, in contrast with its effect in interconnects with non-bamboo polygranular structures, the presence of Cu was shown to have no effect on the failure modes or the times to failure in bamboo Al(Cu) lines, consistent with previous experimental observations.

These failure mechanism maps can now be used to assess reliability at service conditions. Uncertainties associated with scaling of current-density and temperature can be avoided, and circuits can be designed to take advantage of transitions in failure modes with changes in length and current-density.

Thesis Supervisor: Carl V. Thompson
Title: Stavros Salapatas Professor of Materials Science and Engineering

Acknowledgments

My thesis was influenced by more people than I can name. I thank all my family, teachers, and friends for making a dream come true.

I first met my thesis advisor, Professor Carl Thompson, for about 2 minutes during a conference in Bangalore. For reasons known only to him, he hired me, paid my salary and Lab fees, and motivated my research. He taught me the science of experimentation and the art of doing research, and gave me the freedom to pursue my ideas. He has been supportive even when my progress was excruciatingly slow. In return for all this, I can only offer him my gratitude. I consider him, in every sense of the word, my *Guru*. I shall really miss working with Carl.

Professor Subra Suresh and Professor Samuel Allen graciously agreed to serve on my thesis committee. I thank them, and Professor Eduard Arzt, Professor Harold Frost and Professor Ilan Blech, for suggestions, encouragement, and advice.

Many people have contributed towards my education over the past years, especially my teachers in Bangalore, Varanasi, and Cambridge. The folks at the CMSE Labs, Bldg 13 MicroLab, and the Probe Lab taught me how to fabricate and analyze my samples. I am grateful to Rich, Tim, Gale, Libby, Joe, Peter, and Neel for their patience and help. For friendship and support, many thanks to all my colleagues at the Submicron Materials Group, including Brett, Steve, Walid, Vab, Mauro and Morgan. I am especially grateful to Young-Chang, who spent countless hours teaching me the art of growing single-crystal Al films. It is a pleasure to thank him for his generosity with time and knowledge, and his constant good humor (especially since he was in the midst of finishing experiments and writing a thesis!).

I owe more than I can express to my extended family (Grandparents, Grand-aunts and uncles, cousins, uncles and aunts) in India, for all that I have taken, and continue to take, for granted. Their attitudes towards learning and scholarship have influenced mine to a large extent, and this thesis is as much theirs as mine.

There were some glorious periods in graduate school when ideas flowed fast and

easy, the pressure was 10^{-6} and falling, and the plasma was blue and steady. At such times, MIT is a great place to be, and I shall always treasure my interactions with the wonderful people here.

There were also many periods in the past years when the only good thing about graduate school seemed to be the security of misery! At such times, I repeatedly turned to a few people to help regain my perspectives. Appa and Abbu must be, at a conservative estimate, the coolest parents on Earth and nearby planets, and who said coolness is not genetically transmitted?! 201 Pearl has been a great home thanks to TAV, Ramdas, Rajesh, Mukund, Sankar, Gokul, Pradeep, and by natural extension, Neela, Bhuvana, Sumanth, Rashmi and SRV. Erin, probably the best office-mate in the world, has been a tremendous source of fun and advice (especially on the identification of spurious X-ray intensity!). I am particularly grateful for her careful and critical reading of this thesis. Four hours of laughter and music every week with Lynne and George*ji*'s class helped me survive one particularly horrid semester. It is a great pleasure to thank you folks for friendship, conversations, advice, music, laughter, food, coffee, Jungle Book, phone calls, fights, Yo-Yos, hikes in NH, cakes, movies, and books, among a zillion other things.

I dedicate this thesis to my teachers, academic and otherwise. Happily enough, that covers most everyone I know!

Contents

1 Introduction **14**

1.1 Electromigration 15

1.2 1-d Electromigration Model 16

1.2.1 Assumptions 17

1.2.2 Fluxes and Forces 17

1.3 Effect of Microstructure 19

1.4 Electromigration-Induced Failure 20

1.5 Electromigration Lifetime Tests and Scaling 21

1.6 Circuit Design and Reliability Estimation 22

1.7 Numerical Simulation of Electromigration 22

1.8 Goal and Organization of the Thesis 24

2 Effect of Al_3Ti Overlayers on Electromigration in Single-Crystal Al Interconnects **26**

2.1 Background 26

2.2 Fabrication of Test Structures 27

2.3 Characterization 28

2.3.1 Auger Electron Spectroscopy (AES) 28

2.3.2 X-ray Diffraction: $\theta - 2\theta$ and Rocking Curves 31

2.3.3 Transmission Electron Microscopy (TEM) 34

2.4 Electromigration Tests 35

2.4.1 Joule Heating Measurements 36
2.4.2 Determination of the MTTF and the DTTF 38
2.4.3 Activation Energy for Electromigration Failure 40
2.4.4 Void Morphologies and DTTF 40
2.5 Stress Induced by Phase Transformation 42
2.6 Discussion 44
2.7 Conclusions 45

3 Diffusion and Electromigration of Cu in Single-Crystal Al Lines 46
3.1 Background 46
3.2 Sample Fabrication and Tests 47
3.3 EPMA and GMRFILM 48
3.3.1 Concept of k-ratio 49
3.3.2 The $\Phi(\rho z)$ Correction Procedure 50
3.3.3 The Electron Microprobe 50
3.3.4 GMRFILM 51
3.4 Analysis of Diffusion and Electromigration 52
3.5 Results and Discussion 54
3.5.1 Activation Energy for Diffusion 54
3.5.2 Effect of Surface-to-Volume Ratio 57
3.5.3 Apparent Effective Valence (Z*) 57
3.5.4 Comparison with Literature 61
3.6 Conclusions 62

4 Numerical Simulation of Electromigration-Induced Stress Evolution in Bamboo Al(Cu) Interconnects 63
4.1 Background 63
4.2 Evolution of the State of Interconnects 64
4.3 Details of the Simulation 68

4.3.1 Input Values 68
4.3.2 Definition of Failure 70
4.3.3 Electromigration Failure Maps 72
4.4 Results 73
4.4.1 Electromigration Failure Maps for Al(0.2at% Cu) 73
4.4.2 Electromigration Failure Maps for Bamboo Al 73
4.4.3 Role of Cu in Bamboo Al(Cu) 73
4.5 Discussion 78
4.5.1 Deviation in the Times to Failure 78
4.5.2 Initial Stress in Interconnects 79
4.5.3 Choice of Critical Stresses 80
4.5.4 Utility of Electromigration Failure Maps 81
4.5.5 A New Paradigm for IC Design 81

5 Summary and Future Work **83**
5.1 Summary of Results 83
5.2 Implications of the Results 84
5.2.1 Cu-based Metallization 84
5.3 Future Work 85

A Fabrication of Single-Crystal Electromigration Test Structures **87**
A.1 Epitaxial Al Deposition on NaCl Substrates 87
A.2 Transfer onto Oxidized Si Wafer and Adhesion Anneal 88
A.3 Patterning, Etching and Passivation 89

B Dislocation Model for Slit-like Voids **91**
B.1 Introduction 91
B.2 Existing Models 92
B.3 Role of Dislocation Pile-Ups 93
B.4 Energetic Feasibility of the Mechanism 96

B.5 Effect of Crystallography 97
B.6 Implications of the Model 97
B.7 Conclusion 97

C Mechanical Behavior of Thin Al Films and Lines on Si **98**
C.1 Background 98
C.2 Experimental Procedures 99
C.2.1 Sample Fabrication 99
C.2.2 Wafer-Curvature Measurements 100
C.3 Deformation in Thin Solid Lines 100
C.4 Results 101

Bibliography **103**

List of Figures

1-1 Schematic plan-view of the grain structure and void morphologies in polygranular and bamboo Al interconnects. 21

1-2 Schematic illustration of a layered Al(Cu) interconnect with bamboo grain structure. The surrounding passivation is not shown. 24

2-1 Schematic of the multiline test structure. The reference lines were used to monitor stress voiding. All dimensions are in μm. 28

2-2 Auger electron spectroscopy depth profile of the reacted Ti/Al film showing the existence of two layers. The top layer (low sputter times) contained both Ti and Al, while the next layer contained only Al. The sputter times correspond to sample thickness. 30

2-3 X-ray diffraction analysis of the reacted Al/Ti film, showing the (110)-peak of the Al_3Ti phase. Analysis of the powdered specimen revealed more peaks, confirming phase identification. 32

2-4 Rocking curve diffraction analysis of Al_3Ti/Al bilayer lines, after electromigration testing and thermal cycling. The FWHM is about 1°, indicating lack of extensive polygonization and dislocation generation. 33

2-5 Circuit for constant-voltage electromigration tests. 36

2-6 Increase in temperature due to Joule heating in a single line. All the tests were performed using a current of 14 mA/line. 37

2-7 Schematic illustration of the effect of shunting layers on the current-time plots obtained from electromigration lifetime experiments. . . . 39

2-8 Activation energy for failure of single-crystal Al lines with and without Al_3Ti overlayers. The average error in the lifetimes is $\pm 0.25\ t_{50}$ for both sets of data, and corresponds to a 90% confidence interval. 41

2-9 Stress - Temperature plots for polycrystalline Al thin films with, and without Ti overlayers. The former was isothermally held at 450 ^oC for 2.5 hours to promote the formation of Al_3Ti. 43

3-1 Schematic of the test structure. Measurements of Cu concentration were performed on either side of the source for both sets of lines. . . . 48

3-2 Solutions of Equation (3.4) when v is 1, 0, and -1. The concentration and distance are measured in arbitrary units. 53

3-3 Calculation of the diffusivity by nonlinear regression analysis of Equation(3.4). 55

3-4 Activation energy for diffusion of Cu in single-crystal Al interconnects. Shown for comparison is the corresponding value for diffusion of Cu through the Al lattice [Pet 70]. 56

3-5 The dependence of the effective diffusivity on line width for a 0.4 μm thick single-crystal Al line. 58

3-6 Concentration-profile of Cu for diffusion with, without, and against electric current. The test was conducted at 350 ^oC for 3600 s, using a current-density of 1 MA/cm^2. The solid curves are fits to Equation(3.4) as explained in the text. 59

3-7 Concentration-profile of Cu for diffusion aided by electric current. The test was conducted at 350 ^oC for 2400 s, using a current-density of 1 MA/cm^2. The solid curve is a fit to Equation(3.4). 60

4-1 Nucleation and growth of voids in a metal line ending in blocking boundaries. The shunting layers on the metal line are not explicitly shown [Par 99]. 66

4-2 Change of resistance with time for a metal line subject to electromigration [Par 99]. 67

4-3 Representative interconnect chosen for construction of electromigration failure maps. All dimensions are in μm. 70

4-4 Stress-relaxation zone in the vicinity of a void [Par 99]. 72

4-5 Electromigration failure map for bamboo Al(0.2at%Cu) interconnects at 100 ^oC. Tensile failure corresponds to an increase in resistance by 25%. The unlabeled field corresponds to void saturation. 74

4-6 Electromigration failure map for bamboo Al(0.2at%Cu) interconnects at 100 ^oC. Tensile failure corresponds to a void of length 1 μm. The unlabeled field corresponds to void nucleation-limited failure. 75

4-7 Electromigration failure map for bamboo Al interconnects at 100 ^oC. Tensile failure corresponds to an increase in resistance by 25%. The unlabeled field corresponds to void saturation. 76

4-8 Concentration of Cu along a 200 μm long, bamboo Al(Cu) line subject to electromigration. The numbers on top of each curve indicate time in hours. 77

4-9 Schematic illustration of the effect of initial stress on failure and mode of failure. 80

5-1 Effective resistivity of Al, Cu, and Cu-alloy lines as a function of line width. The lines are assumed to have a square cross-section. 86

B-1 Schematic illustration of the formation of an S-void by the interaction of a translating E-void with a pileup of dislocations. All the grains are (111)-oriented except for the one marked (110). 93

B-2 Schematic illustration of a slip plane in an interconnect containing dislocations. 94

C-1 Curvature - Temperature plot for 3 μm wide, 0.8 μm thick lines. . . . 101

List of Tables

4.1 Physical and Material Constants Used in the Simulations 70

4.2 Transport Parameters Used in the Simulations 71

A.1 Parameters for etching Al 90

A.2 Parameters for depositing PECVD SiO_2 90

A.3 Parameters for etching PECVD SiO_2 90

B.1 Critical Resolved Shear Stress (τ) 96

Chapter 1

Introduction

Microelectronics has profoundly influenced humanity in the latter half of the 20th century, revolutionizing travel, communication, entertainment, computation, and warfare. At the heart of this revolution lies the ability to design and fabricate integrated circuits (ICs), the first of which was manufactured by Kilby at Texas Instruments in 1958. Prior to this, electronic equipment consisted of discrete devices (such as transistors, resistors, and capacitors) wired together onto circuit boards. This procedure was both costly and unreliable. Using a thin wafer of germanium, Kilby demonstrated that all these devices could be fabricated from the same material. The later development of the IC, however, followed the work of Hoerni and Noyce at Fairchild Semiconductor Corporation. They fabricated the first planar transistor by selectively doping chosen parts of a silicon wafer. The first planar IC consisted of four transistors and five resistors, connected by thin wires of deposited Aluminum [Aug 83].

From such modest beginnings, modern ICs have evolved into extraordinarily complex systems, containing more than a million transistors, which must be appropriately connected to function properly. First, all the devices are electrically isolated by passivating the silicon surface with a dielectric layer (usually SiO_2). Contact cuts are etched in the dielectric at chosen regions, and a thin conducting film (usually Al(Cu)) deposited over the wafer. This alloy film is subsequently patterned into a large num-

ber of narrow lines, which link the appropriate devices, completing the circuit. These metal lines are referred to as *interconnects.* Modern ICs contain more than five levels of metallization by a repetition of this process. In an IC occupying the surface of a 1 cm^2 Si chip, there can be more than 10 meters of total interconnect length, in the form of more than a *million* line segments. During the operation of an IC, interconnects carry current densities as high as 0.5 MA/cm^2 (compared to a maximum of 100 A/cm^2 allowed in household wiring). While the Si substrate is a good heat sink, interconnects can still experience temperatures of the order of 100 - 125 °C during operation. In addition, thermal cycling during production and operation can result in thermal mismatch stresses greater than 500 MPa in the interconnects. There is an ever-increasing demand for circuits with smaller interconnect dimensions (< 0.2 μm), which allows for greater integration and higher speeds of operation. This, in turn, means that the interconnects carry higher current densities, operate at higher temperatures, and experience greater mechanical stresses.

Under such extreme conditions of operation, interconnects are susceptible to failure due to a phenomenon called electromigration, first identified by Blech and Sello in 1967 [Ble 67]. Since the failure of any one of the million line segments can lead to failure of the IC, understanding and predicting electromigration-induced failure in interconnects is of crucial importance. Building upon past research, this thesis is an attempt at predicting electromigration-induced failure in one microstructural class of interconnects, namely those with *bamboo* grain structures.

1.1 Electromigration

Electromigration is atomic diffusion influenced by the motion of electrons. Under an applied electric field, the thermally activated diffusion of atoms in a metal or alloy can be biased by two opposing forces. The first is the electrostatic response of the atom or ion to the applied field. The second is the transfer of momentum from the

conducting electrons to the atoms or ions. In interconnect systems of interest, the latter dominates and mass transport occurs towards the positive electrode. The force ($\mathbf{F}_e$) applied by the *electronic wind* on atomic species i can be expressed as:

$$\mathbf{F}_{e,i} = Z_i^* e\mathbf{E} = Z_i^* e\rho_i \mathbf{j}, \tag{1.1}$$

where e is the fundamental charge, $\mathbf{j}$ is the current density, $\mathbf{E}$ is the applied electric field, ρ is the resistivity, and Z^* is an empirically determined *effective valence* [Hun 61, Fik 59]. This form of the equation is convenient since the general formalism of field-enhanced diffusion can be used. The values of Z^* of constituent atoms in Al-alloy interconnects have been empirically determined to lie in the range -1 to -100, and are weakly dependent on composition, microstructure, temperature, and current-density. Electromigration, and the resultant damage, in interconnects has been the subject of intense study over the past two decades. A short, but delightful, account of the pioneering work in the field is contained in [Llo 96]. Several volumes of the Materials Research Society's Symposium Proceedings are dedicated to this topic (*Materials Reliability in Microelectronics*, Vol. I to VIII). Recent reviews include [ThL 93, Hu 95].

1.2 1-d Electromigration Model

The most widely accepted description of electromigration in encapsulated metal lines is an one-dimensional model, originally formulated by Blech and Herring to describe the steady state [Ble 76], and extended to include transients by Korhonen *et al.* for one-component systems [Kor 93]. The implicit assumptions of this model were clarified by Clement and Thompson [Cle 95]. Korhonen *et al.* then proposed a generalized version, formulated in the spirit of irreversible thermodynamics, which has the advantage of being independent of the exact mechanisms of diffusion and can be easily extended to multi-component systems [Kor 95]. This is a particularly attrac-

tive feature, since alloys are commonly used as interconnect materials. This analysis was generalized and implemented in a numerical scheme by Park *et al.* [Par 99], as summarized below.

1.2.1 Assumptions

1. The interconnect is idealized as an one-dimensional line segment, embedded in a rigid matrix. Gradients of all quantities are hence interpreted as spatial derivatives with respect to the coordinate along the line length.
2. The stress state of the interconnect is hydrostatic (σ).
3. The alloy is a substitutional solid solution of two atomic species A and B, both of which have similar atomic volumes (Ω).
4. Joule heating, temperature gradients, and thermomigration are ignored.
5. The vacancy concentration is in equilibrium with the stress. This implies the existence of sources and sinks for vacancies such as internal interfaces and dislocations.
6. The number of atoms in the interconnect is conserved at all times.
7. The diffusivity and effective valence are treated as scalar quantities.

1.2.2 Fluxes and Forces

The gradients in chemical, electrical, and mechanical potentials give rise to forces on the atoms, and in turn, to a flux of matter. The force due to the electric field is expressed by Equation (1.1). Following Herring [Her 50], the force due to gradients in the hydrostatic stress ($\mathbf{F}_\sigma$) on atomic species i can be expressed as

$$\mathbf{F}_{\sigma,i} = -\Omega \nabla \sigma. \tag{1.2}$$

The force due to the chemical interaction ($\mathbf{F}_\mu$) is a function of the nature of the solid solution. In general, if μ_i is the chemical potential, then

$$\mathbf{F}_{\mu,i} = -\nabla\mu_i. \tag{1.3}$$

The total force on each atomic species ($\mathbf{F}_i$) is the sum of the individual driving forces. These forces give rise to fluxes ($\mathbf{J}_i$), linearly related via phenomenological coefficients (L) as

$$\mathbf{J}_A = L_{AA}\mathbf{F}_A + L_{AB}\mathbf{F}_B, \tag{1.4}$$

$$\mathbf{J}_B = L_{BA}\mathbf{F}_A + L_{BB}\mathbf{F}_B. \tag{1.5}$$

The Onsager relations are not obeyed since $\mathbf{J}_A$ and $\mathbf{J}_B$ are not independent, and hence $L_{AB} \neq L_{BA}$ [You 82]. Neither L_{AB} nor L_{BA} is known for the alloy system of interest (Al-Cu), and will be ignored in further analysis. As an approximation then, we have for the flux of each atomic species i,

$$\mathbf{J}_i = \frac{D_i C_i}{kT}(\mathbf{F}_i). \tag{1.6}$$

Here D is the effective diffusivity, C is the atomic concentration, k is Boltzmann's constant, and T is the absolute temperature. Conservation of mass requires the continuity equation

$$\frac{\partial C_i}{\partial t} = \gamma - \nabla.\mathbf{J}_i, \tag{1.7}$$

where γ is the rate of change of the vacancy concentration. A change in the relative density of confined metal lines gives rise to a change in the stress that can be expressed as

$$d\sigma = -B\frac{dC}{C}, \tag{1.8}$$

where B is an effective bulk modulus, and $dC = \Sigma dC_i$ is the change in the number of

lattice sites per unit volume [Kor 93].

Equations (1.6), (1.7), and (1.8) form a complete set for numerical integration of electromigration-induced stress evolution. The general form of these equations is independent of the details of the transport mechanisms; these mechanisms affect only the kinetics of stress evolution, and depend on the microstructure.

1.3 Effect of Microstructure

The effective atomic diffusivity depends on the details of the microstructure of the interconnect. In the most general case, diffusion can occur through the metal lattice, down dislocation cores, along the interfaces of the interconnects and its surrounding matrix, and along grain boundaries. The effective diffusivity (D) can be expressed as

$$D = D_L + A_d \rho_d D_d + 2D_i \delta \alpha_i \left(\frac{1}{w} + \frac{1}{h}\right) + \frac{D_{gb} \delta \alpha_{gb}}{d_{50}}, \tag{1.9}$$

where D_L, D_d, D_i, and D_{gb} are the diffusivities through the lattice, dislocation cores, interfaces, and grain boundaries, respectively. It is possible, in principle, for all the four interfaces to have different diffusivities. A_d is the cross-sectional area of the dislocation core and ρ_d is the density of dislocations in the interconnect oriented along the line length. The width and thickness of the interconnect are represented by w and h respectively, δ is the width of the diffusive path along the interfaces and grain boundaries, and α is the segregation coefficient. d_{50} is the median grain size of the interconnect line.

The grain structure of annealed interconnects changes from polygranular to bamboo as their width decreases below the median grain size of the film from which they were etched [Wal 92]. The polygranular lines have a continuous network of high diffusivity grain boundaries along their length, and electromigration occurs primarily through this path. The bamboo interconnects, however, have all their grain boundaries oriented perpendicular to the line length, and hence also to the applied electric

field. Hence, transgranular transport becomes dominant in such structures, leading to lower electromigration kinetics and longer times to failure [Vai 80, Cho 89].

An expression analogous to Equation(1.9) applies for the effective valence as well.

1.4 Electromigration-Induced Failure

Electromigration of atoms and the resultant buildup of mechanical stress can lead to different types of failure in interconnects. Depletion of matter can result in formation of voids, resulting in an open-circuit failure if they span the width of the line. Often, interconnects are fabricated with refractory shunting layers (such as TiN and Al_3Ti). In such structures, spanning voids do not necessarily lead to open-circuits, and failure is defined as an increase in resistance beyond a specified value.

Associated with the change in grain structure from polygranular to bamboo is a change in the morphology of voids. In polygranular lines, voids typically nucleate and grow at grain boundary triple points, and are termed *erosion voids*. The dimensions of the sides of the erosion voids are comparable to the width and thickness of the line. In bamboo lines, erosion voids can also appear as edge-voids, elongated along the line length. In addition, another morphology, *slit-like voids*, is also seen [San 92, Ros 92]. The slit-like voids tend to grow almost perpendicular to the length of the line, and have a thickness of the order of 0.1 μm. The erosion voids are often the precursors to the slit-like voids, as elaborated in Appendix B.

A schematic illustration of the microstructure and void morphologies in polygranular and bamboo interconnects is shown in Figure 1-1.

Accumulation of atoms can lead to an increase in the compressive stress, and ultimately to cracking of the dielectric passivation and the shunting layers. This can result in extrusion of the metal, potentially causing short circuit connections with adjacent interconnects.

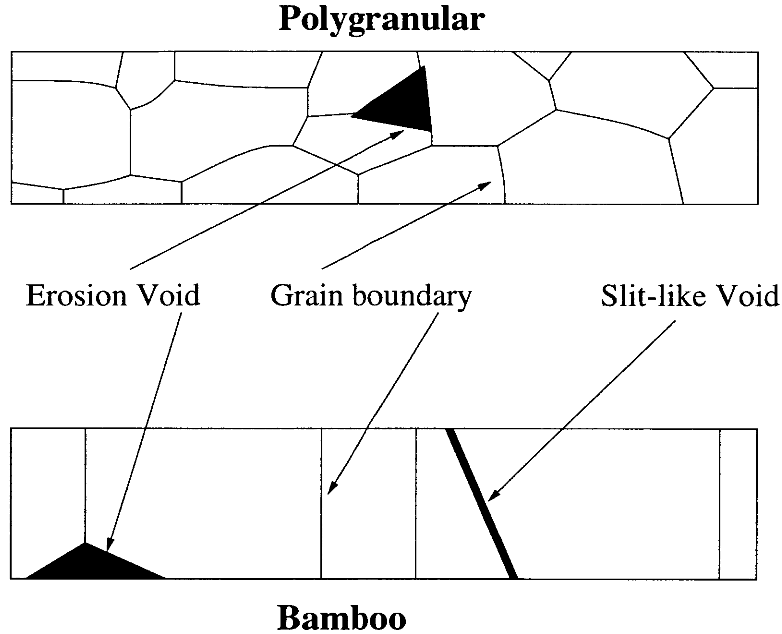

Figure 1-1: Schematic plan-view of the grain structure and void morphologies in polygranular and bamboo Al interconnects.

1.5 Electromigration Lifetime Tests and Scaling

Electromigration is a slow and stochastic process. Hence, tests to failure are performed at accelerated temperatures and current densities on populations of lines. The resulting failure times are assumed to follow the log-normal distribution (the logarithm of the failure times are normally distributed), and the median and deviation in the times to failure (MTTF and DTTF respectively) can be computed. This information has to be then scaled down to service conditions, and this is usually done by using Black's equation [Bla 67]

$$t_{50} = Aj^{-n}\exp(\frac{Q}{kT}), \tag{1.10}$$

where t_{50} is the MTTF, A is a materials constant, and Q is the appropriate activation energy. Traditionally Q has been assumed to represent the activation energy for long

range diffusion. The exponent on the current-density, n, assumes a value of 1 if failure is dominated by growth of voids, and a value of 2 if failure is dominated by the nucleation of voids. This scaling law was proposed based on empirical observations, and significant deviations have been documented under a variety of conditions [Kno 97].

1.6 Circuit Design and Reliability Estimation

Design rules for interconnects are formulated based on data from accelerated tests and are usually very conservative, leading to reduced performance. In some cases, these rules can severely overestimate lifetimes, potentially causing failure of electronic components. An alternate evolving paradigm for circuit design is to couple the design process with accurate reliability estimation using three computational tools: ERNI, GGSim, and MIT/EmSim [Demo 98]. ERNI extracts the interconnects from the circuit layout, and bins them according to geometry, boundary conditions, and the details of the direct current passing through them. The interconnects are present not only as straight lines, but also in more complex shapes, such as L, T and I. They can also be linked to each other forming *interconnect trees.* GGSim simulates the evolution of the grain structure in these patterns as a function of materials, processing and geometry. Finally, electromigration-induced stress evolution, and hence the reliability of interconnects, can be predicted using MIT/EmSim. Such an approach can lead to the fabrication of ICs with greater reliability and better performance.

1.7 Numerical Simulation of Electromigration

Numerical simulation of electromigration-induced stress development is a robust method for predicting the reliability of interconnects, since much of the uncertainty associated with accelerated testing can be removed by performing simulations at service conditions.

Numerical solution of the set of equations (1.6, 1.7, and 1.8) requires the knowledge of

1. *Boundary conditions*: The most common boundary condition is one where the atomic flux is completely blocked (zero-flux), either due to refractory layers, W-studs, or due to contacts to Si. Accelerated testing is sometimes performed on lines terminating in large contact pads, leading to zero-stress boundary conditions at either end of the interconnect.

2. *Physical and materials constants*: Boltzmann's constant (k), electronic charge (e), atomic volume (Ω), resistivity (ρ), and effective modulus (B).

3. *Test conditions*: Temperature (T) and current-density (j).

4. *Initial condition*: This refers to the state of mechanical stress in the line prior to the application of the electric field. Intrinsic stresses, thermal mismatch between the metal and its matrix, and phase transformations in layered interconnects are the causes for this stress. Interconnects confined by a rigid passivation are usually under a triaxial state of stress. For the solution of the 1-d model, the description of the hydrostatic stress is sufficient, and can be calculated for a specified thermal history [Gou 98].

5. *Transport parameters*: The effective diffusivity (D) and effective valence (Z^*) for each atomic species.

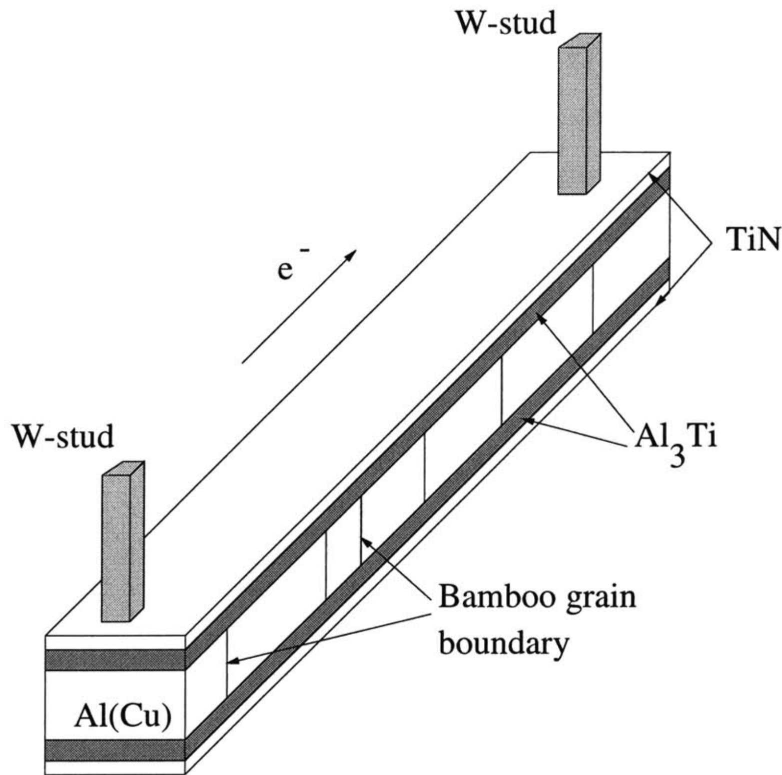

Figure 1-2: Schematic illustration of a layered Al(Cu) interconnect with bamboo grain structure. The surrounding passivation is not shown.

1.8 Goal and Organization of the Thesis

With increasing miniaturization and reducing feature sizes, a large number of interconnects in ICs have bamboo grain structures. Passivated Al(Cu) lines with bamboo microstructures, clad with TiN and Al_3Ti layers, and terminating in W-studs are commonly encountered in most Al-based metallization schemes. A schematic illustration of such an interconnect is shown in Figure 1-2. The goal of this thesis is to provide the knowledge of the transport properties required to simulate electromigration-induced stress evolution, and hence the reliability, of such interconnects. The transport properties of Al and Cu in bamboo Al(Cu) lines can be unambiguously determined by conducting experiments on single-crystal Al lines.

Previous work on Al single-crystal lines (covered with AlO_x on all sides) has indicated that the path for atomic transport is along the Al/AlO_x interfaces [Joo 97]. Modern interconnects are covered at the top and bottom with refractory layers such as Al_3Ti, and the effects of such layers on electromigration in bamboo Al lines are unknown. Chapter 2 describes experimental studies of electromigration in Al single-crystal interconnects capped with Al_3Ti layers.

Small amounts of Cu can increase the reliability of polygranular Al lines by two or three orders of magnitude, and modern Al interconnects contain about 0.5 wt% Cu in them. However, the effects of Cu on bamboo Al lines and the transport properties of Cu in such interconnects are unknown. Chapter 3 describes experiments to determine the diffusivity and effective valence of Cu in Al single crystals.

Chapter 4 describes simulation of electromigration-induced stress evolution in bamboo Al and Al(Cu) lines. Such simulations can elucidate the effects of Cu on bamboo Al(Cu) lines. Further, these simulations can also be used to construct electromigration *failure maps*, which are plots of current-density versus line length showing domains of dominance of different failure modes. Such maps can be readily used to estimate the reliability of interconnects.

Chapter 5 contains a summary of the results of the previous chapters, along with a discussion of their implications with regard to the design of reliable interconnects. This chapter also contains suggestions for future research.

Chapter 2

Effect of Al_3Ti Overlayers on Electromigration in Single-Crystal Al Interconnects

2.1 Background

The kinetics and mechanisms of electromigration-induced failure are strongly dependent on microstructure. In lines with bamboo grain structure, diffusion and electromigration occur via transgranular mechanisms through the lattices of the bamboo grains, down dislocation cores, or along the interfaces between the metal and its surrounding matrix. Uncertainty remains as to which mechanism dominates. Oates conducted drift experiments on submicron, bamboo lines and reported that the drift velocity and the activation energy are consistent with transport through the Al lattice [Oat 96]. Joo and Thompson performed electromigration lifetime tests using single crystal Al interconnects, and obtained an activation energy of about 1.0 eV in both passivated and unpassivated lines [Joo 97]. The activation energy for self-diffusion of Al has been the subject of some controversy, and measured values lie in the range 1.2 to 1.4 eV. Peterson and Rothman have argued that the activation energy for

self-diffusion through the Al lattice over a wide temperature range (85 ^oC to 625 ^oC) is 1.26 eV [Pet 70]. Since the measured activation energy is significantly less than 1.26 eV, Joo and Thompson concluded that diffusion along the Al/AlO_x interface dominates in single-crystal and bamboo Al interconnects.

Refractory layers are commonly present at the interfaces between the Al lines and the surrounding dielectric. Currently, Al_3Ti and TiN are used at the top and bottom interfaces of Al alloy interconnects, and act as diffusion barriers, anti-reflection coatings, and as current-shunting layers for improved reliability. The effects of these layers on the kinetics and mechanisms of electromigration-induced failure are not known, but can be unambiguously determined by conducting experiments on single-crystal Al lines capped with Al_3Ti layers.

2.2 Fabrication of Test Structures

4500 $\AA$ thick single-crystal films of Al were fabricated on oxidized Si wafers as described in Appendix A. The orientation of the Al crystal was such that the (110) crystallographic planes were parallel to the substrate. The films were then loaded into a MRC Sputtering System and pumped down to a base pressure of 10^{-6} torr. The chamber was subsequently pressurized with 5 mtorr of Ar, and the native Al-oxide etched using a power of 200 watts for 6 minutes. This was immediately followed by deposition of Ti for 5 minutes at the same power, without an interruption of the vacuum. The thickness of the deposited Ti was about 300 $\AA$. This metallic bilayer was covered with 2000 $\AA$ of sputtered SiO_2 and annealed in a vacuum of 10^{-7} torr, for 1 hour at 450 ^oC, to promote the formation of Al_3Ti. The SiO_2 was subsequently stripped, and the interconnect lines defined and passivated with 2500 $\AA$ of PECVD SiO_2. The lines were 1 mm long, 2.0 μm wide, and terminated in large contact pads [Tho 86]. The average number of lines per test was ten, and the crystallographic orientation along the line length was [110]. This structure (Figure 2-1) is identical to

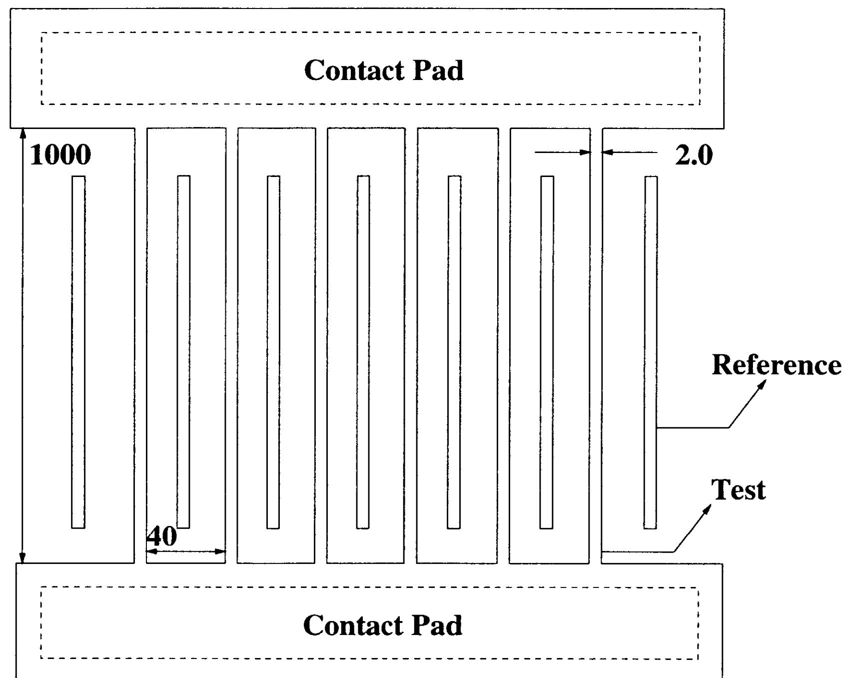

Figure 2-1: Schematic of the multiline test structure. The reference lines were used to monitor stress voiding. All dimensions are in μm.

the ones used by Joo and Thompson [Joo 97], except for the presence of the Al_3Ti capping layer.

2.3 Characterization

The chemistry, crystallography, geometry, and microstructure of the reacted films were characterized before and after electromigration testing.

2.3.1 Auger Electron Spectroscopy (AES)

The interaction of energetic electron-beams with inorganic solids can result in the emission of electrons and photons. For ease of description, consider an element whose K, L, and M shells are populated by electrons. If the incident beam ejects an electron

from the inner K shell, the resultant relaxation can occur in one of two modes. The first is the generation of characteristic X-rays due to the transition of an outer shell electron (L or M) into the K shell. These characteristic X-rays form the basis for X-ray spectroscopy. The second mode is the generation of Auger electrons, where the energy released by the electronic transition to the K-shell results in the ejection of an electron from the outer shell, leading to a doubly-ionized atom. The energies of these Auger electrons have an one-to-one correspondence with atomic number, giving rise to the possibility of Auger electron spectroscopy.

The Auger electrons as well as the characteristic X-rays are generated throughout the interaction volume, whose dimensions can be of the order of microns. However, the sampling volumes for the analytical signals are vastly different. The characteristic X-rays are not significantly affected by inelastic scattering processes while passing through the sample towards the detector. They are either completely absorbed through photoelectric effects, or they reach the detector with the same characteristic energy with which they were created. The Auger electrons, in contrast, continuously undergo energy loss through various inelastic scattering processes as they pass through the sample. The only electrons which retain their initial energy are those generated in the surface layers. The AES signal is hence a surface-sensitive signal with a depth resolution of about 1 nm [Gol 92].

It is possible to obtain a depth profile of the entire sample by progressively removing atom layers by sputtering with an ion beam in stages, and performing AES at each stage. The sensitivity to surface conditions requires that the entire analysis be carried out in ultra-high vacuum (pressures lower than 10^{-9} torr). A Phillips 660 Scanning Auger Microprobe was used to obtain AES depth profiles, under analysis conditions of 5 kV and 50 nA, using a spot-size of 1 μm.

As shown in Figure 2-2, the analysis revealed the presence of two layers, one which contained Al and Ti, and the other which contained, within detection limits, only Al.

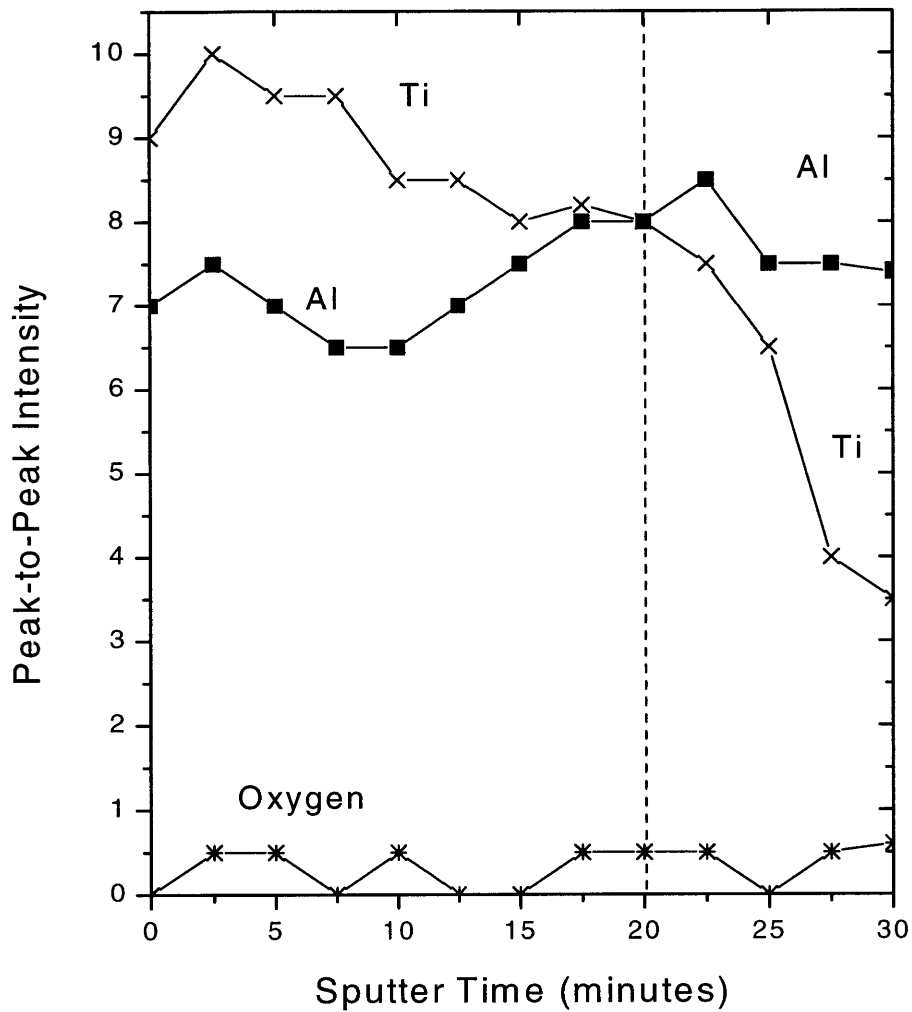

Figure 2-2: Auger electron spectroscopy depth profile of the reacted Ti/Al film showing the existence of two layers. The top layer (low sputter times) contained both Ti and Al, while the next layer contained only Al. The sputter times correspond to sample thickness.

No oxygen was detected at any stage of the analysis, indicating the absence of oxidation of either layer.

The sputter-time corresponds to the thickness of the bilayer. However, the dimensions of the two layers could not be determined due to the lack of good thin film standards.

2.3.2 X-ray Diffraction: $\theta - 2\theta$ and Rocking Curves

X-ray diffraction analysis was performed using a Rigaku 300 diffractometer, with a rotating Cu anode, operated at 60 kV and 300 mA. The crystallography and the nature of the phases present in the reacted films were characterized in the standard $\theta - 2\theta$ geometry. The (110) peak of Al and (110) peak of Al_3Ti were identified. The latter is shown in Figure 2-3. Analysis of the powdered sample revealed more peaks, confirming identification of the Al_3Ti phase.

In order to monitor the extent of subgrain formation in the Al single crystal, rocking curve diffraction was performed on the (110) peak of the Al. The rocking curve is obtained by fixing the detector at the 2θ value of the peak of interest, and allowing the value of θ to change in a chosen range. The width of the rocking curve is a direct measure of the range of orientations present in the irradiated area of the crystal, since each subgrain successively satisfies the Bragg condition as the crystal is rotated [Cul 78].

Rocking curves were obtained on Al single crystals before and after the reaction with Ti, and after electromigration testing. In all cases, the full-width at half-maximum intensity (FWHM) was less than 1° (Figure 2-4), indicating that the formation of subgrain boundaries was not extensive. This, in turn, indicates that the dislocation density was invariant in these single crystals during thermal cycling, phase reaction, and electromigration testing.

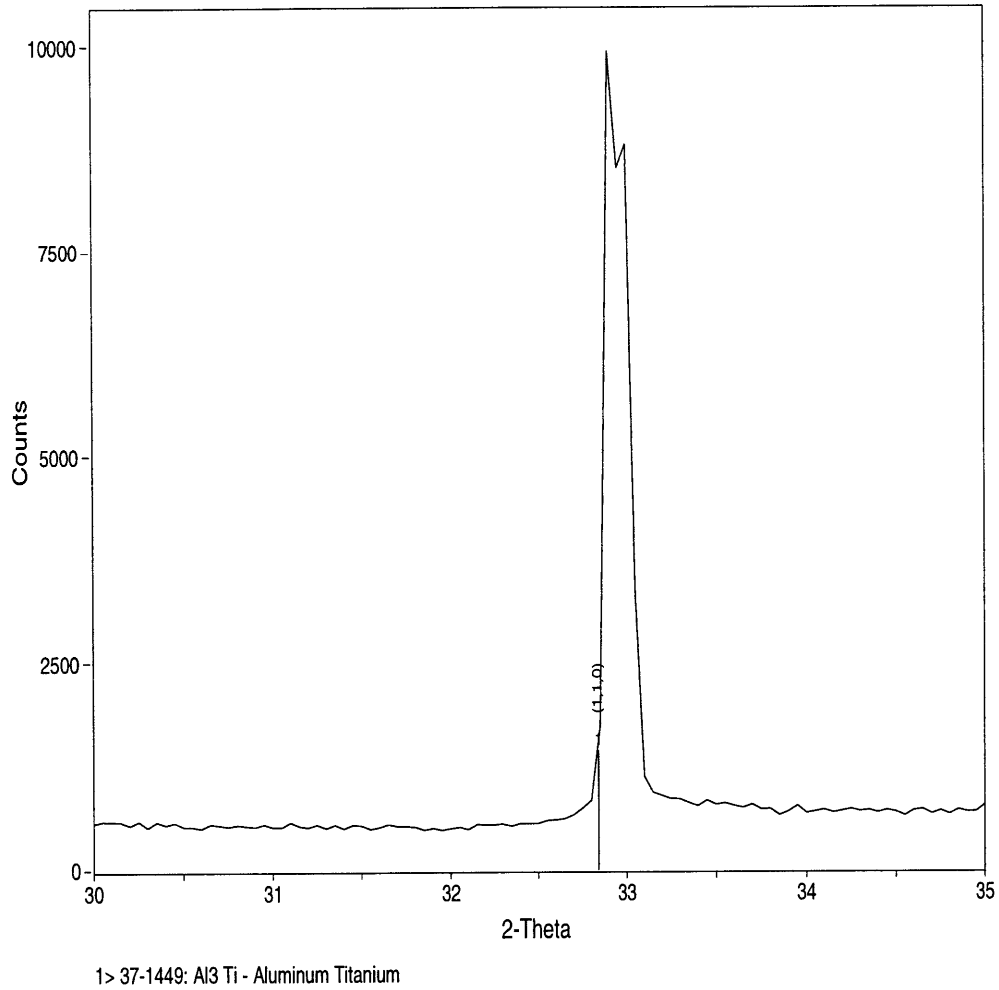

Figure 2-3: X-ray diffraction analysis of the reacted Al/Ti film, showing the (110)-peak of the Al_3Ti phase. Analysis of the powdered specimen revealed more peaks, confirming phase identification.

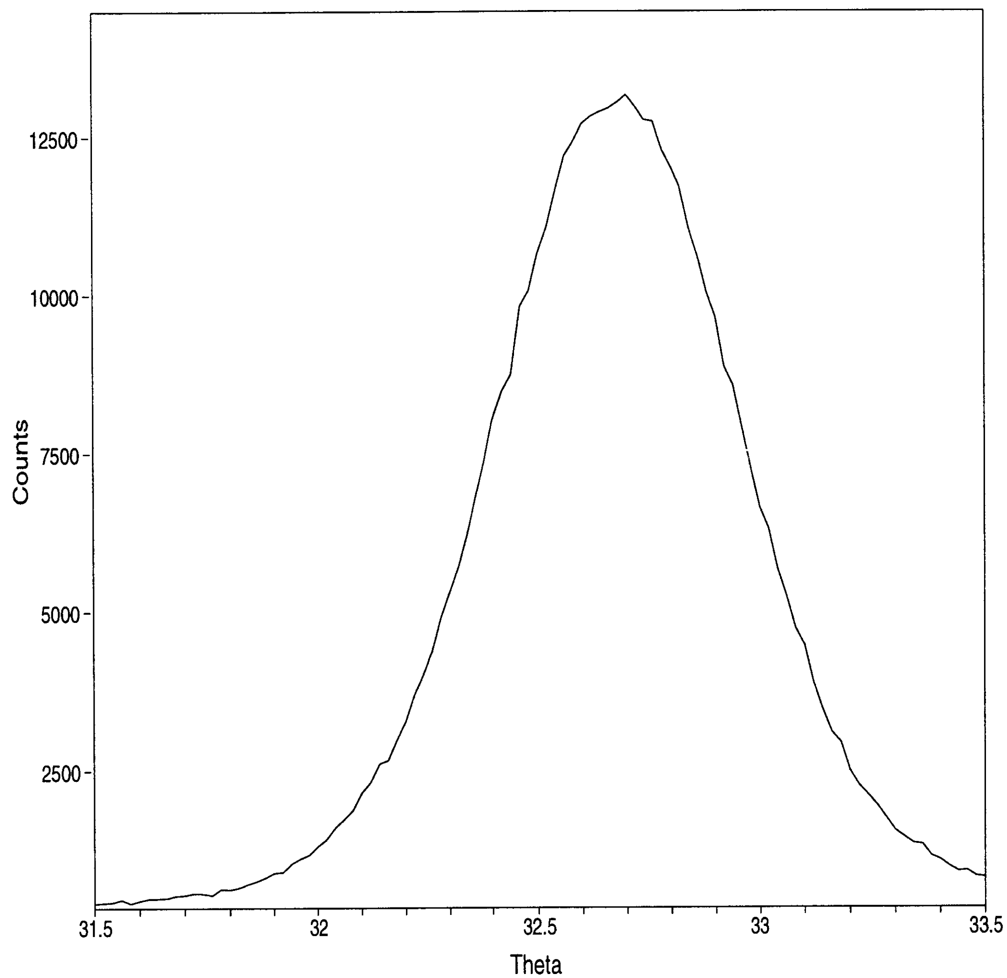

Figure 2-4: Rocking curve diffraction analysis of Al_3Ti/Al bilayer lines, after electromigration testing and thermal cycling. The FWHM is about 1°, indicating lack of extensive polygonization and dislocation generation.

2.3.3 Transmission Electron Microscopy (TEM)

The experiments described in this section were performed at Digital Equipment Corporation in collaboration with Bill and Miner [Min 97]. The principal objective of this analysis was to study the nature of the two metallic phases, and also that of the interface between them. It was hence necessary to prepare an electron-transparent foil that contained a vertical cross-section of the test structure.

This cross-section was prepared using a Tripod Polisher^{TM} (South Bay Technology, Inc.) as described in detail in [Ben 92]. The sample was first cleaved through the center of the test structure, such that the lines terminated at the cleaved end. This was then mounted on a Tripod Polisher, and mechanically polished on one side using a sequence of progressively finer grit diamond lapping films. The same surface was then briefly polished on a cloth wheel with colloidal silica to obtain a final polish. The sample was then flipped over, remounted, and polished using the same sequence of diamond lapping films. The polishing was done such that the final sample is wedge shaped, with the areas of interest being at the thinnest edge of the taper. The polishing was stopped when the thin end was electron transparent.

Analysis was performed in a Philips CM30 TEM at 300 kV, and micro-diffraction of the cross-section confirmed the identification of the Al_3Ti phase, and also revealed that the Al_3Ti was present as a smooth, continuous, polycrystalline layer, about 500 $\mathring{A}$ in thickness. The thickness of the Al was about 3800 $\mathring{A}$, which is consistent with measurements of the electrical resistivity.

While the reaction between polycrystalline Al and Ti thin films has been extensively studied [Col 90], this is the first such study where the Al is a single crystal, and there are a few interesting deviations from the polycrystalline Al case.

(i) The Al_3Ti layer that we obtained was quite smooth, while that obtained from pure, polycrystalline Al can be quite rough. This roughness is probably due to the action of Al grain boundaries as sites for nucleation of Al_3Ti.

(ii) The orientation relationship obtained was (110) Al_3Ti/(110) Al, while (112)

Al_3Ti/(111) Al is usually obtained using polycrystalline films. This difference in crystallography is unlikely to affect the electromigration lifetime, since there appears to be very little dependence of the diffusivity on crystallography in Al single crystal interconnects [Joo 98].

(iii) Microvoids ($<$ 12 nm in diameter) were observed at the interface between Al and Al_3Ti. These probably form as a result of the supersaturation of the vacancy concentration due to the diffusion of Al to react at the Al_3Ti/ Ti interface. There have been no reports of such voids in polycrystalline films, possibly because the Al grain boundaries serve as sinks for the vacancies. If these voids affect the rate of electromigration at all, it is expected that they should lead to enhanced kinetics in these single crystals, compared to conventional bamboo lines. The results of the lifetime tests will therefore serve as an upper bound of the impact of Al_3Ti overlayers on the kinetics of electromigration in Al_3Ti-clad bamboo interconnects.

In addition, low-angle grain boundaries were observed in one of several TEM samples, possibly having resulted from the polygonization of Al. However, as described earlier, X-ray rocking curves indicate that this process was not extensive, and was not affected by accelerated electromigration testing. The details of the electromigration tests are presented in the next section.

2.4 Electromigration Tests

Constant-voltage electromigration lifetime tests were performed at different temperatures in the range 360 °C to 400 °C, using a constant current density of 1.75 MA/cm^2. An HP model 6253 DC power supply was used as a voltage source to maintain a constant voltage across the terminals, and the current was monitored as a function of time, as shown in Figure 2-5.

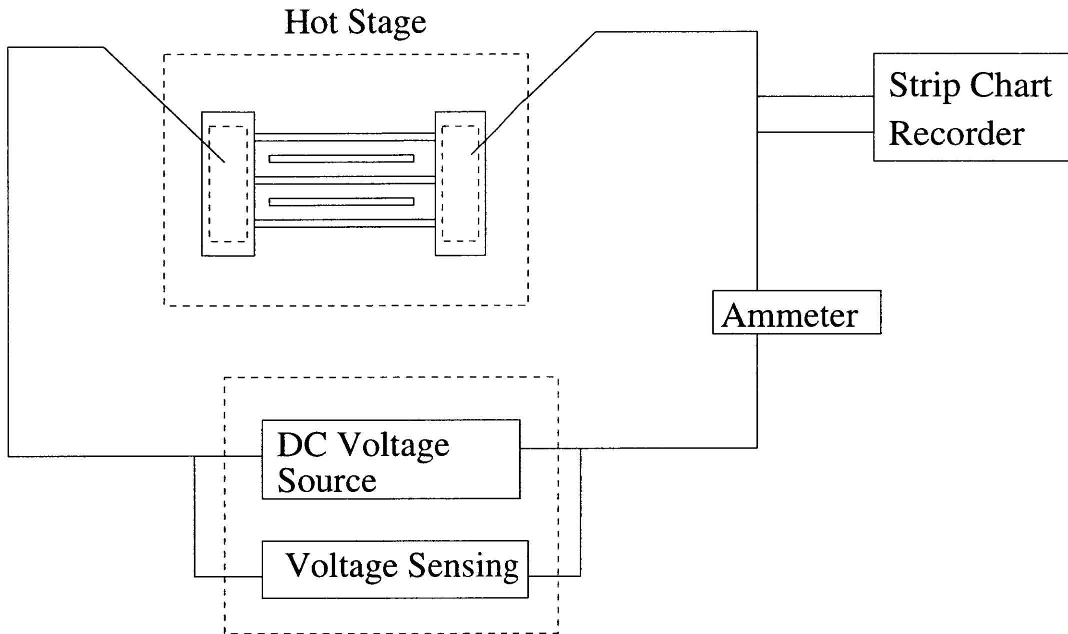

Figure 2-5: Circuit for constant-voltage electromigration tests.

2.4.1 Joule Heating Measurements

Testing at high current densities can result in significant Joule heating of the interconnects. More importantly, the increase in temperature is highly non-uniform along the length of the lines, since the pads act as heat sinks. This can induce a non-zero divergence in the mass flux, since the diffusivities are strong functions of the temperature. To minimize such effects, the increase in temperature due to Joule heating was never allowed to exceed 10 ^oC. In addition to current-density, the increase in temperature depends on geometry, presence of shunts and encapsulation, test temperature, and number of lines tested. The temperature increase must hence be measured for each test structure.

A convenient method of measuring Joule heating is to monitor the resistance of the test structure. If the resistance at temperature T_i is R_i, then

$$R_2 = R_1(1 + \alpha(T_2 - T_1)), \tag{2.1}$$

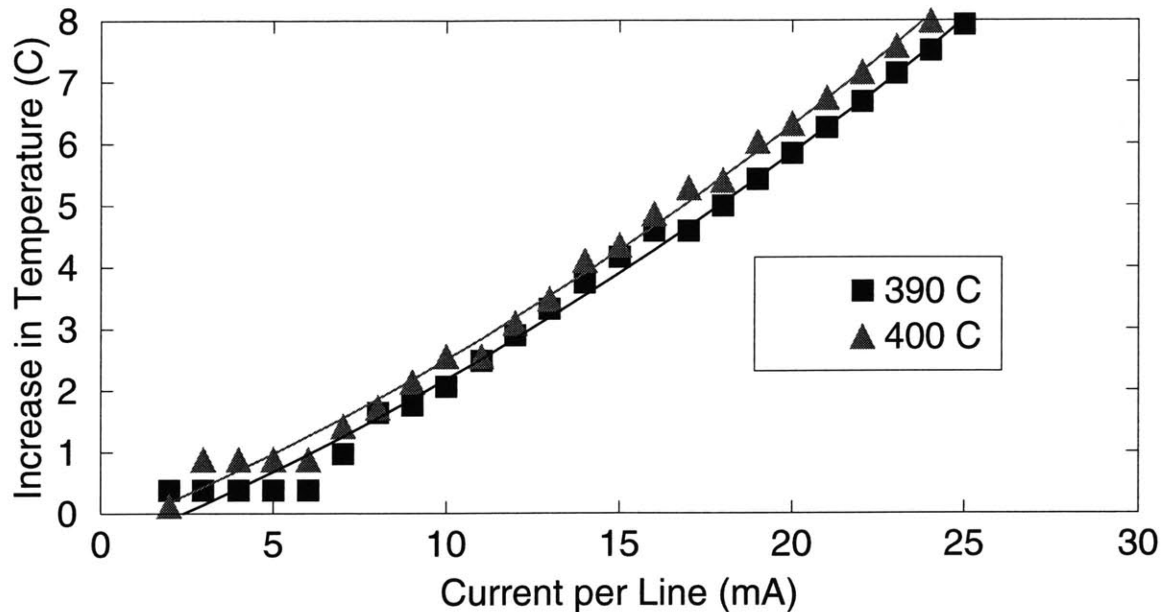

Figure 2-6: Increase in temperature due to Joule heating in a single line. All the tests were performed using a current of 14 mA/line.

where α is the temperature coefficient of resistance. α was measured to be 3.6 x $10^{-3}/^{o}$C, by determining the resistance change at various substrate temperatures, using very low currents to eliminate Joule heating effects. Figure 2-6 shows the increase in temperature for a single line structure at 400 ^{o}C and 390 ^{o}C as a function of the current. All the electromigration tests were performed using a current of 14 mA/line. For a single line structure, this corresponds to an increase in temperature of about 4 ^{o}C as shown in Figure 2-6. Similar measurements were performed on each structure used, and the maximum increase in temperature was less than 10 ^{o}C. The test temperature was defined to be the sum of the temperature of the hot-stage and the average temperature increase due to Joule heating [Coo 94].

2.4.2 Determination of the MTTF and the DTTF

While the use of a multi-line test structure allows for simultaneous testing of many lines at each test condition, it prohibits the determination of the time to failure of any particular line. For unlayered lines, the current-time plot obtained from a constant-voltage test exhibits a discontinuous change every time any one line fails or heals [Tho 86]. The failure times can be fit to a lognormal distribution, and the statistical parameters (median time to failure (MTTF) and deviation in time to failure (DTTF)) obtained using well defined procedures.

In contrast, the presence of Al_3Ti shunting layers prevent open-circuit failure of the layered lines. Hence, when a void develops in the interconnects, the current shunts through the capping layers, which have a higher resistivity compared to Al. The increased resistance causes a corresponding decrease in the current in these constant-voltage experiments. The individual failure times and their distribution cannot therefore be identified. We *assumed* that the failure times follow a lognormal distribution, with the MTTF and the DTTF suitably defined as follows. If t_n be the time taken for the current to decrease by n% of its initial value, then the median time to failure is defined as t_{50} and the deviation in the time to failure is defined as $\ln(t_{50}/\ t_{16})$.

The current-time plots for layered and unlayered lines are schematically indicated in Figure 2-7.

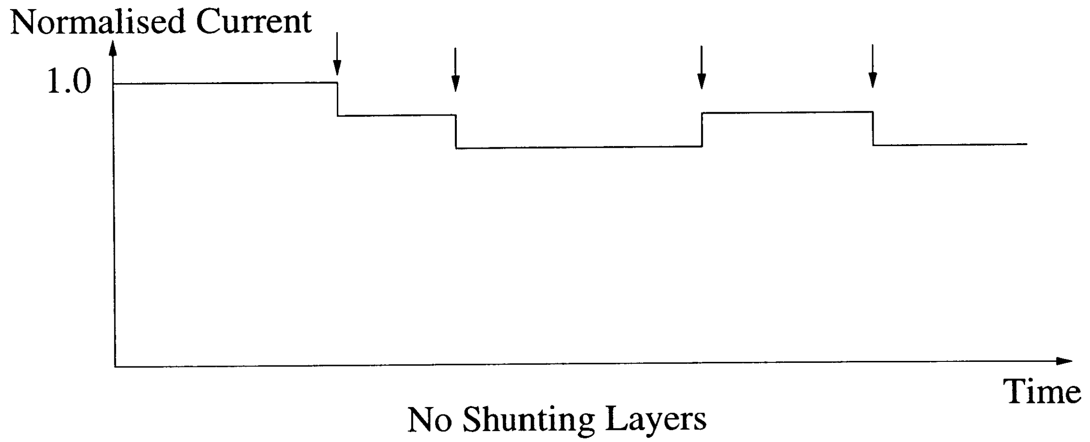

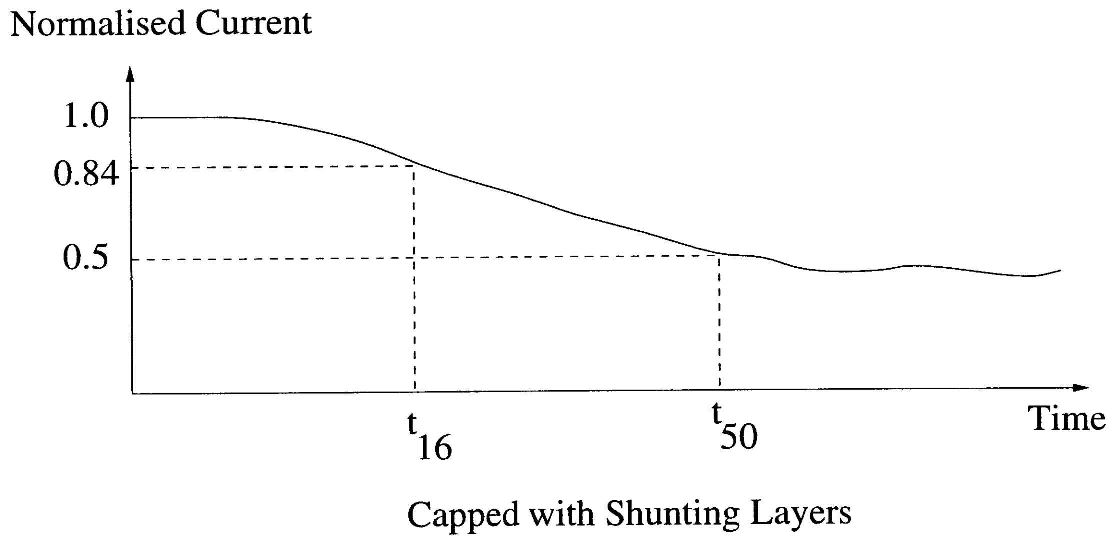

Figure 2-7: Schematic illustration of the effect of shunting layers on the current-time plots obtained from electromigration lifetime experiments.

2.4.3 Activation Energy for Electromigration Failure

The activation energy was calculated assuming that the failure times follow an Arrhenius behavior, expressed by Equation(1.10). The plot of the median time to failure as a function of the reciprocal of the absolute temperature is shown in Figure 2-8. The activation energy can be calculated from the slope, and was found by linear regression analysis to be 0.94 ± 0.05 eV. The correlation-coefficient of the best-fit line was 0.99.

The same plot shows the lifetimes and activation energy for single crystal lines without Al_3Ti overlayers [Joo 97]. These experiments were performed using a current-density of 2.5 MA/cm^2, and were hence rescaled to 1.75 MA/cm^2 to enable comparison. The scaling was performed using Equation(1.10), assuming a value of 2 for the exponent n. This comparison shows that the activation energy is unaffected by the presence of Al_3Ti capping layers. In addition, the MTTF in layered lines is about 1.5 times the corresponding value in lines without Al_3Ti capping layers.

2.4.4 Void Morphologies and DTTF

An extensive study of void morphologies in single-crystal Al interconnects was conducted by Joo and Thompson [Joo 97]. Two distinct void morphologies were found to exist: *erosion voids* and *slit-like* voids. As the names suggest, erosion voids typically are wedge-shaped, and have sides with dimensions comparable to the line width and thickness. The slit-like voids, on the other hand, tend to grow almost perpendicular to the line length, and are often very narrow in width (< 1 μm). The existence of these two failure modes resulted in very high values of the DTTF (~ 1.0) in the experiments of Joo and Thompson.

The DTTF was found to be about 0.5 in the present experiments on the layered lines. This can be directly attributed to the presence of the shunting layers, since slit-like voids cause a very small increase in the resistance of the lines, and only the formation and growth of erosion voids lead to a significant decrease in the current.

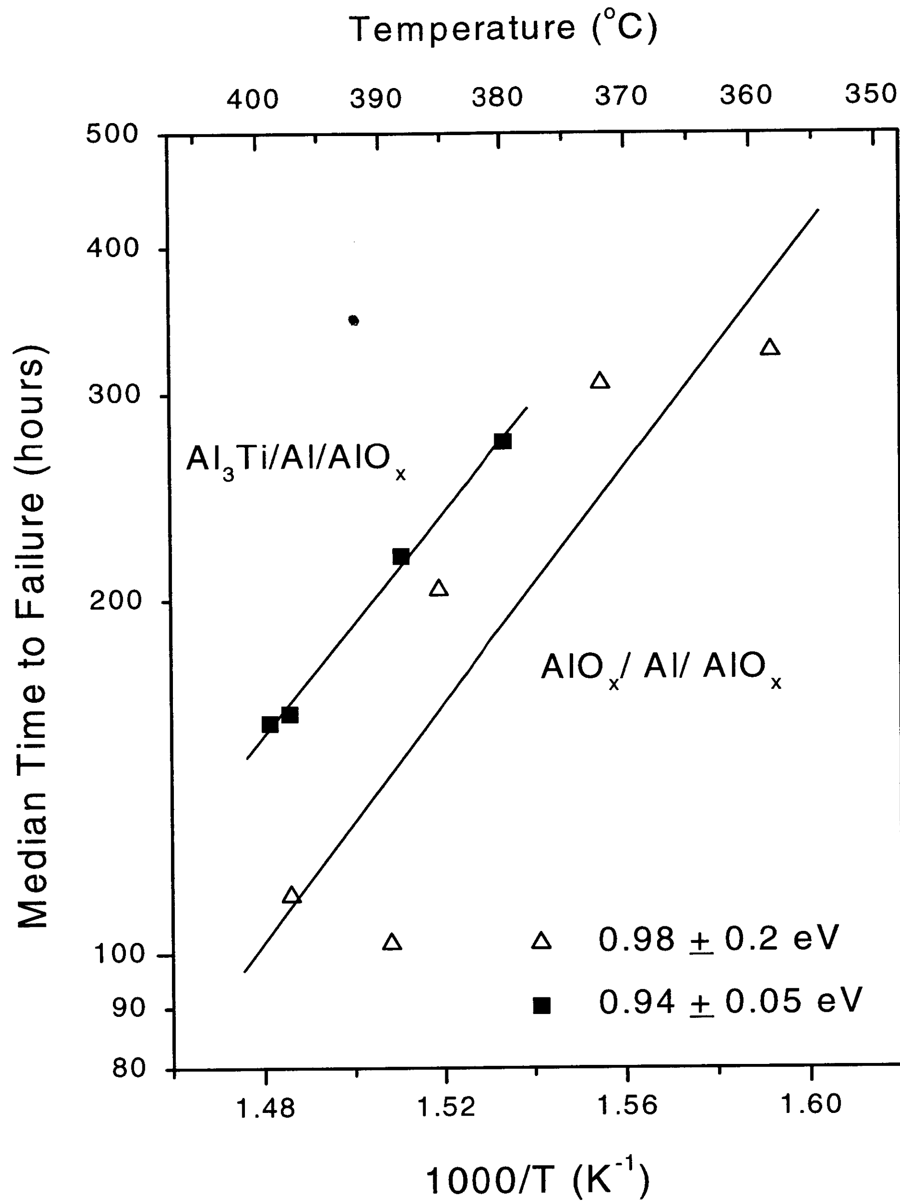

Figure 2-8: Activation energy for failure of single-crystal Al lines with and without Al_3Ti overlayers. The average error in the lifetimes is $\pm 0.25\ t_{50}$ for both sets of data, and corresponds to a 90% confidence interval.

2.5 Stress Induced by Phase Transformation

One potential difference between the structures used in the present study, and those used by Joo and Thompson [Joo 97], is the role of mechanical stresses induced by the reaction to form Al_3Ti. Appendix C contains a discussion of the nature, origin, and measurement of such stresses.

In order to study the effects of the Al_3Ti overlayers, two sets of samples were fabricated. The first contained 0.6 μm thick, polycrystalline Al films, sputter-deposited on oxidized Si substrates. For the second set, the deposition of Al was followed by the deposition of 0.05 μm of Ti, without an interruption of the vacuum. Films from both sets were cycled between 50 ^oC and 450 ^oC at 6 ^oC/minute. In addition, those films containing Ti were isothermally held at 450 ^oC for 2.5 hours to promote the reaction of Al and Ti to form Al_3Ti. The cycling was performed in a reducing atmosphere and the formation of the Al_3Ti phase was confirmed by X-ray diffraction.

The stresses in the films were monitored during thermal cycling by wafer-curvature measurements, and are shown in Figure 2-9. The stress-temperature response for pure Al is shown by the discontinuous line.

The solid line represents the response of the Ti/Al bilayer, and shows an increase in the tensile stress at the reaction temperature. The subsequent shape of the stress-temperature plot, however, resembles that of pure Al.

During the reaction, the dimensions and nature of the film stack change, along with stress relaxation in the films (for example, by dislocation glide). To get an upper bound on the effects of the stress on the transport of Al, let us assume that the change in curvature is entirely due to the stress in the Al film. This leads to an estimated increase in tensile stress of about 100 MPa. Further, let us assume that this results in an increase of 100 MPa in the hydrostatic stress in the lines. We can now estimate the maximum change in the diffusivity of Al due to the formation of the Al_3Ti layer.

Let D_o and D_σ be the diffusivities at stresses zero and σ respectively. Then,

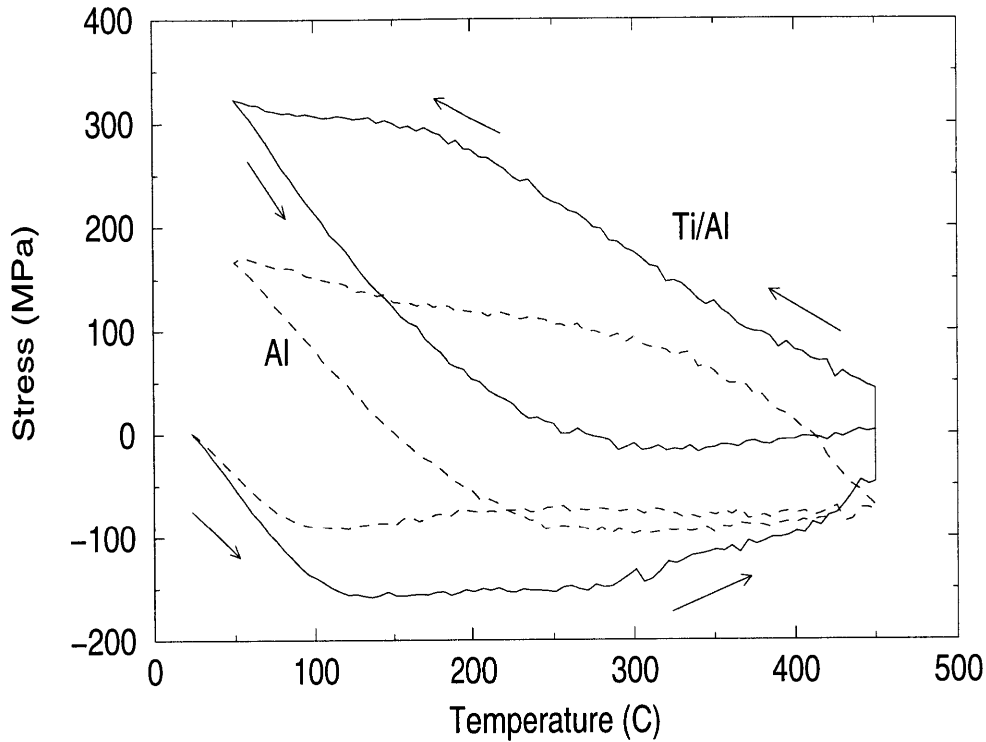

Figure 2-9: Stress - Temperature plots for polycrystalline Al thin films with, and without Ti overlayers. The former was isothermally held at 450 ^oC for 2.5 hours to promote the formation of Al_3Ti.

assuming a vacancy mechanism for diffusion [Cle 95],

$$\frac{D_\sigma}{D_o} = exp\left(\frac{\Omega\sigma}{kT} + \frac{\sigma}{B}\right). \tag{2.2}$$

Using values of 1.6 x 10^{-29} m^3 and 50 GPa for the atomic volume and effective modulus, an increase in stress of 100 MPa changes the diffusivity by a factor of 1.2 at 350 ^0C.

Hence, we conclude that the stress induced by phase reaction does not affect the kinetics of diffusion and electromigration.

2.6 Discussion

The comparison of lifetime data for clad and unclad single crystal interconnects is only approximate as explained earlier. However, the comparison of the activation energies is exact, since consistent criteria were followed in both cases.

The activation energy for electromigration-induced failure as determined by lifetime tests can correspond either to the activation energy of the dominant diffusion mechanism for long-range transport of the metal, or to the activation energy of processes involved in the failure itself, such as creep of the dielectric, nucleation of voids, or deformation of the metal, for example through dislocation climb. If the measured activation energy corresponds to that of the dominant diffusion mechanism, this mechanism cannot be lattice diffusion, since the activation energy for lattice diffusion is significantly higher, 1.26 eV [Pet 70]. Similarly, it cannot be diffusion of Al through the Al_3Ti, which is expected to have an activation energy of 1.8 eV [Tar 85].

Oates has shown that dislocation cores allow much less flux of matter than the lattice at 200 ^oC, even for dislocation densities as high as $10^{10}/\ cm^2$, with all the dislocations oriented with their lengths parallel to the electric field [Oat 96]. This conclusion is valid for all temperatures greater than 200 ^oC, since the activation energy for core diffusion is 0.85 eV [Vol 71]. The TEM and X-ray analyses conducted on the single crystal lines indicate dislocation densities far lower than $10^{10}/cm^2$. Furthermore, these dislocations tend to lie perpendicular to the line length, and hence also to the applied electric field, in these highly annealed lines.

It was postulated by Suo that dislocations can climb and multiply in response to the electron-wind [Suo 94]. However, as shown earlier, no evidence of increased dislocation density resulting from electromigration tests was found. It is hence concluded that no dislocation-based mechanism contributes to the mass-flux in single crystal lines.

Having eliminated mechanisms for bulk diffusion, and if the measured activation energy does correspond to the activation energy for diffusion, it is concluded that this

must be interfacial diffusion. The similarity of the activation energy and lifetimes for clad and unclad single-crystal lines requires that Al diffusivity along the Al/Al_3Ti interface be the same as, or lower than, the diffusivity of Al along the Al/AlO_x interface, throughout the temperature range of these experiments. This interpretation is surprising, especially given the presence of the microvoids at the Al/Al_3Ti interface, but also with the qualitative expectation that diffusion along the Al/Al_3Ti metal-metal interface should be similar to grain-boundary diffusion.

An alternate interpretation for the similarities of the lifetimes and failure kinetics in clad and unclad single-crystal lines is that the measured activation energy is not characteristic of the long-range diffusion mechanism but is instead characteristic of a yet unknown failure process common to both types of samples.

2.7 Conclusions

Al_3Ti capping layers do not significantly impact the kinetics of electromigration in Al single crystals. If the measured activation energy corresponds to the activation energy for diffusion, then the results suggest that the diffusivity of Al along the Al/ Al_3Ti interface is lower than, or equal to, the diffusivity of Al along the Al/AlO_x interface. Alternately, the activation energy for electromigration-induced failure may correspond to a yet unknown failure process.

Chapter 3

Diffusion and Electromigration of Cu in Single-Crystal Al Lines

3.1 Background

One of the most successful methods of increasing the electromigration lifetimes of Al interconnects was discovered at IBM in 1970. Ames, d'Heurle, and Horstmann found that a small amount of Cu (< 4 wt%) could increase the median time to failure of Al conductors by 2 to 3 orders of magnitude [Ame 70]. The most popular explanation for such a dramatic increase in reliability is that Cu inhibits the self-diffusion of Al along the grain boundaries, which dominate atomic transport in these wide, polygranular lines. The rate of electromigration-induced failure would therefore be limited by the rate of electromigration of Cu along Al grain boundaries.

Howard and Ross developed an experimental technique for determining the diffusivity and rate of electromigration of Cu in polygranular Al lines, in which a cross-stripe structure is fabricated with Al and Cu lines patterned perpendicular to one another [How 71]. This creates a localized source of Cu in the middle of the Al lines. Ho and Howard used such structures to quantitatively determine the diffusivity and effective valence of Cu along the grain boundaries in Al, by analyzing the concen-

tration profile of Cu after electromigration in these structures [Ho 74]. Such values are of crucial importance in estimating electromigration-induced stress evolution, and hence the reliability, of interconnects.

Since these early experiments, Al(Cu) alloys have been widely used as interconnect materials. However, as dimensions of interconnects decrease with continued scaling of the ICs, the grain structure evolves from polygranular to bamboo. The effect of Cu on electromigration-induced damage of bamboo Al(Cu) interconnects is not known. In particular, the transgranular transport properties of Cu have not been determined. Unambiguous determination of D and Z* of Cu in bamboo Al can be made by conducting experiments on single-crystal Al lines.

3.2 Sample Fabrication and Tests

4000 $\AA$ thick, (110)-oriented, Al single crystal films were fabricated on oxidized Si wafers. The test structure consisted of 5 μm wide parallel lines, with every alternate one terminating in contact pads, as shown in Figure 1 [Tho 86]. The longer lines were 1 mm long, and the shorter lines 0.8 mm long. The structure was then passivated with 3500 $\AA$ of PECVD SiO_2, as described in Appendix A. By a suitable sequence of etching and passivation, a window was opened in the passivation in the middle of the lines. This structure was then loaded into a MRC Sputtering System, and pumped down to a base pressure lower than 10^{-6} torr. The chamber was then pressurized with 5 mtorr Ar, and the native AlO_x sputter etched for 6 minutes at 200 watts. Without interrupting the vacuum, Cu was deposited for 20 s at the same power. The test structure was then annealed in an Ar atmosphere, at 320 ^oC for 2 minutes, to allow the incorporation of Cu into the Al. The excess Cu was selectively removed using a wet etch (APS etchant, Transene Co. MA). The amount of Cu in the source was chosen to be well above the solubility limit at the temperatures of interest ($<$ 400 ^oC), and Cu is hence present both in solid solution, and as Al_2Cu precipitates.

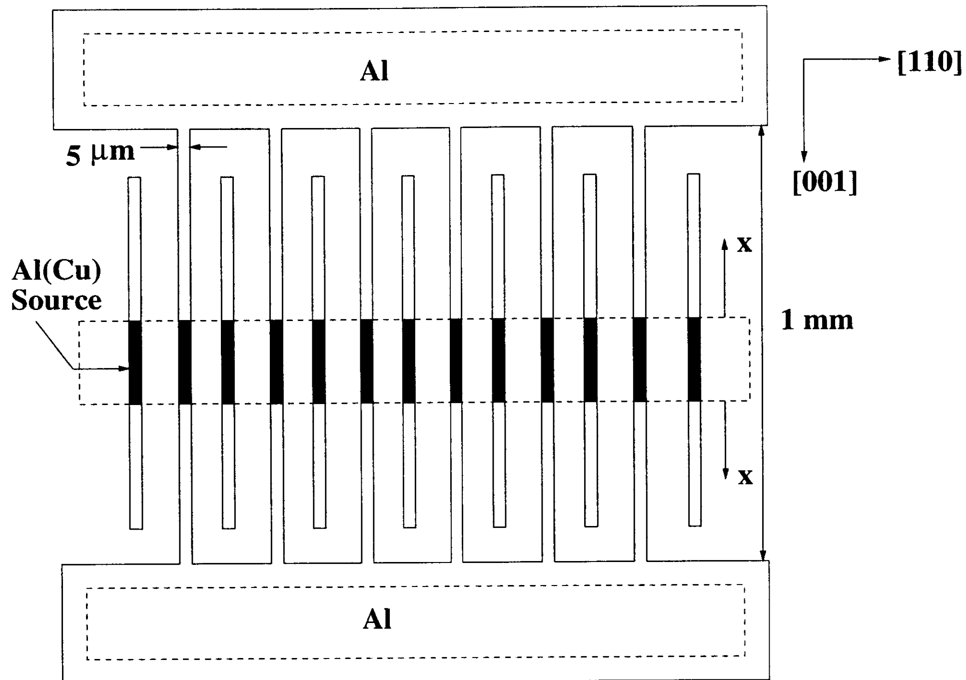

Figure 3-1: Schematic of the test structure. Measurements of Cu concentration were performed on either side of the source for both sets of lines.

The extent of lateral diffusion outside the source was measured to be less than 5μm at the end of the annealing treatment.

Diffusion tests were performed in the temperature range 320 ^{o}C to 400 ^{o}C, and two electromigration tests at 350 ^{o}C, using a current-density of 1 MA/cm^2. The variation in the temperature of the hot-stage was a maximum of $\pm$1 ^{o}C during the experiments. The passivation was then stripped using a selective wet etch (Silox-Vapox, Transene Co. MA), and the Cu profile was measured using wave-length dispersive spectroscopy using electron-probe microanalysis (EPMA).

3.3 EPMA and GMRFILM

Electron probe micro-analysis (EPMA) allows for non-destructive quantitative chemical analysis of microscopic volumes of solid, inorganic materials. The basic idea

behind this technique can be traced back to 1913, when Moseley discovered that the frequency of emitted characteristic X-rays is a function of the atomic number of the emitting element. Marton and Hillier patented the idea of using a focused electron beam to excite characteristic X-rays in a small volume for the purpose of X-ray spectrometry. Castaing and Guinier designed and built the first electron microprobe in 1951, as a part of Castaing's doctoral dissertation. Extensive details on the principles, design, use, and applications of this technique may be found in [Gol 92].

3.3.1 Concept of k-ratio

The most common technique of microanalysis is to use pure elemental standards of various elements to excite X-rays, and to compare these with the spectrum generated from the sample, *under the same conditions.* Castaing noted that the primary generated X-ray intensities are roughly proportional to the respective mass-fractions of the emitting elements. Hence,

$$\frac{C_i}{C_{(i)}} = \frac{I_i}{I_{(i)}} = k_i, \tag{3.1}$$

where C_i and $C_{(i)}$ are the weight concentrations of element i in the sample and standard respectively, and I_i and $I_{(i)}$ are the primary generated X-ray intensities in the sample and standard respectively. However, an element in its own lattice is expected to behave differently when it is placed in a matrix composed of other atomic species. This requires corrections to Equation (3.1), often referred to as *matrix corrections.* This includes absorption in the matrix (A), generation of secondary X-rays by fluorescence (F), and atomic number (Z) corrections. Electron backscattering is dependent on the average atomic number of the target, and is included in the Z-correction. Hence,

$$\frac{C_i}{C_{(i)}} = [ZAF]_i \frac{I_i}{I_{(i)}} = [ZAF]_i k_i. \tag{3.2}$$

In general, the correction factors are dependent on the composition of the sample

being analyzed. Therefore, these analyses are performed iteratively. One convenient method of applying these corrections, especially for thin films, is to use the $\Phi(\rho z)$ procedure.

3.3.2 The $\Phi(\rho z)$ Correction Procedure

The depth-distribution function for X-ray production is termed $\Phi(\rho z)$, and can be thought of as a histogram giving the relative number of X-rays generated in a slice of the specimen of thickness dz, and density ρ. The histogram is normalized by the number of X-rays that the beam would produce in a free-standing layer of the same thickness and composition. The upper layers of the interaction volume between the e-beam and the specimen always produce more X-rays than free-standing layers since the incident electrons can interact with more atoms when they suffer backscattering. As the depth increases, however, the electrons lose their energy due to inelastic scattering and produce less X-rays. $\Phi(\rho z)$ curves are modeled through semi-empirical or empirical fits to measured data. These curves can be directly related to the ZA correction factors [Cha 98], and combined with fluorescence corrections to translate the k-ratios to compositions.

3.3.3 The Electron Microprobe

A JEOL JXA-733 Superprobe was used to acquire the k-ratios, using an accelerating voltage of 15 kV, beam current of 10 nA, and a beam spot size of 1 μm. The sample chamber was maintained at a pressure in the range 2 x 10^{-5} - 10^{-6} torr. Wavelength dispersive spectroscopy was performed using lithium fluoride and thallium acid phthalate crystals, with a take-off angle of 40°. The take-off angle is the angle between the specimen surface and the emergent X-ray traveling toward the analyzing crystal, and is fixed by the design of the instrument. AlK_α and CuK_α line intensities were monitored using counting times of 100 s per analysis. The stepping distance between measurements was 2 to 5 μm. Pure Al and pure Cu bulk standards were

used as references to obtain the k-ratios, which were then translated into compositions using GMRFILM.

3.3.4 GMRFILM

If the interaction volume were to be contained completely in the Al thin film being analyzed, the standard procedures used for bulk specimens can be used. Unfortunately, at an accelerating voltage of 15 kV, the interaction depth is in excess of 1 μm [Gol 92], significantly larger than the thickness of the Al film (0.4 μm). Hence, GMRFILM , a program for analysis of layered samples was used to convert the k-ratios into compositions.

GMRFILM is a public-domain FORTRAN program authored by Waldo at General Motors Research Laboratories [Wal 98]. The $\Phi(\rho z)$ correction scheme introduced by Pouchou and Pichoir [PaP 90] is utilized, along with rigorous characteristic and continuum X-ray fluorescence corrections. In the present case, the use of the program is greatly simplified since the elements of interest (Al and Cu) are confined only to the top-most layer. Further, the composition and thickness of the subsequent layers is known (1000 $\mathring{A}$ of SiO_2 and 525 μm of Si).

The input to the program includes the number of layers present, thickness of layers (if known), elements present in each layer, take-off angle, beam voltage, and k-ratios. Using an iterative process, the compositions and thickness of the unknown layer are calculated. The time for convergence is typically on the order of a few seconds on most computers.

The accuracy of the measurement was confirmed by analyzing a sputtered Al(Cu) thin film of known composition and thickness. The errors in composition are of the order of 0.1 wt% in the vicinity of 1.0 wt%.

3.4 Analysis of Diffusion and Electromigration

Diffusion and drift in one dimension can be described by

$$\frac{\partial c}{\partial t} = D\frac{\partial^2 c}{\partial^2 x} - v\frac{\partial c}{\partial x}, \tag{3.3}$$

where c is the concentration at position x and time t, D is the effective diffusivity, and v is the electromigration drift velocity. This form of the equation assumes that neither D nor v is a function of the concentration. The solution of this equation, for an infinite source at x = 0, and a semi-infinite diffusion zone for x > 0, is

$$c = c_o(1 - erf(\frac{x - vt}{2\sqrt{Dt}})), \tag{3.4}$$

where c_o is the concentration of the source, which is the solubility of Cu in Al at the test temperature. The effective electromigration drift velocity, v, can be expressed as

$$v = \frac{D}{kT}Z^* e\rho j. \tag{3.5}$$

The drift velocity is positive when drift is in the direction of diffusion, negative when drift opposes diffusion, and zero in the absence of an electric field.

As confirmed by EPMA, the source contained Cu well in excess of the solubility limit at the end of the tests, and the diffusion zone is much shorter than half the line length. In order to analyze the concentration profile using Equation (3.4), a planar diffusion profile must be obtained across the cross-section of the lines. In these single-crystals, the possible diffusion paths are the lattice or interfaces. (Dislocation cores can be neglected as possible mass transport paths due to the extremely low density of dislocations oriented along the line length). If the lattice dominates, a planar profile is guaranteed. On the other hand, if the interfacial transport dominates, a planar profile will be obtained as long as the lattice diffusion length is much longer than half the line thickness. Using the value of the diffusivity of Cu through the Al

lattice determined by Peterson and Rothman [Pet 70], the time-spans of these tests were chosen to satisfy this condition. Equation(3.4) is hence an exact solution for the analysis of the present measurements, subject only to the assumption that the diffusivity and effective valence are not functions of Cu concentration. It can also be obtained as a limiting case of a more general treatment based on Whipple's analysis as shown in an analysis of grain boundary transport [Gup 78]. Figure 3-2 shows solutions to Equation(3.4) assuming c_o, $2\sqrt{D}$, and t to be equal to unity, and when the drift velocity is 1, 0, and -1 (all quantities are measured in arbitrary units).

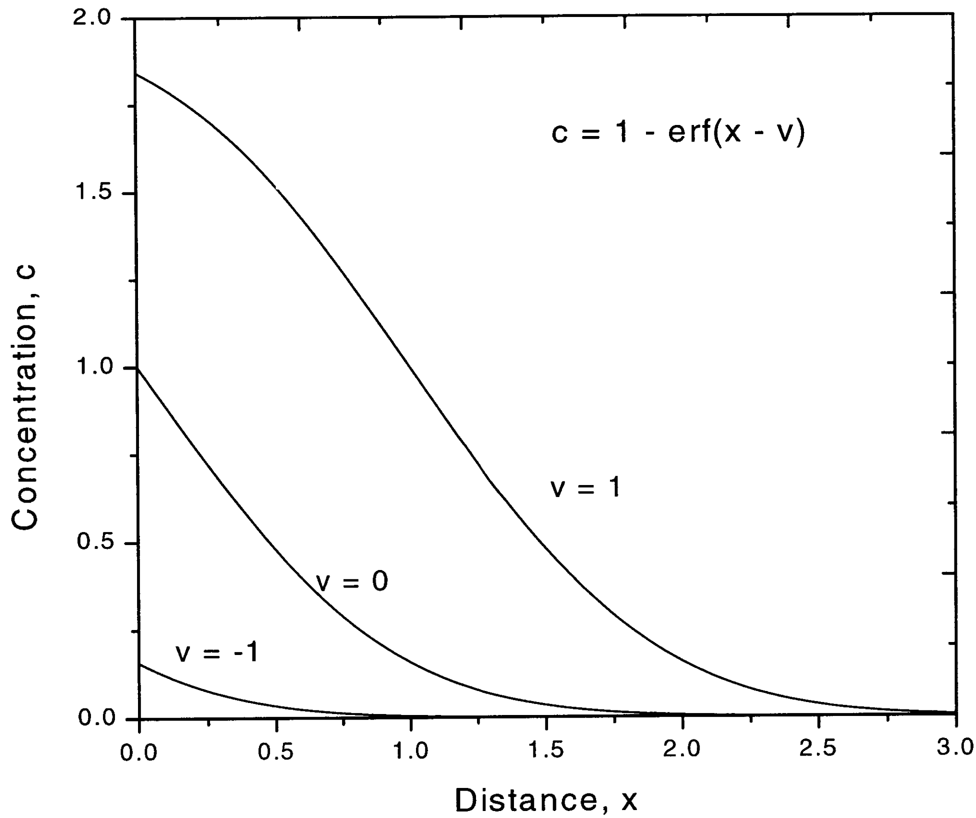

Figure 3-2: Solutions of Equation (3.4) when v is 1, 0, and -1. The concentration and distance are measured in arbitrary units.

3.5 Results and Discussion

3.5.1 Activation Energy for Diffusion

The concentration profiles were fit to Equation (3.4), using the *NonlinearRegress* routine in MATHEMATICA (Wolfram Research, Incorporated). Figure 3-3 shows the analysis of one diffusion test performed at 383 ^{o}C for 4500 s. Each value of the concentration is the average of six different measurements.

Similar curves were obtained, and the diffusivities calculated, at different temperatures in the range 320 ^{o}C to 400 ^{o}C. The Arrhenius plot of the diffusivities as a function of the reciprocal of the absolute temperature is shown in Figure 3-4. The indicated error bars for the diffusivities correspond to a 95% confidence level. The activation energy was determined by linear regression to be 0.8 $\pm$ 0.2 eV. The correlation-coefficient of the best-fit line was 0.84. Also shown in the same plot is the diffusivity of Cu through the Al lattice, which has an activation energy of about 1.4 eV [Pet 70]. This comparison suggests that the Al lattice does not play a significant role in the transport of Cu in these single-crystals. By a process of elimination, it is concluded that the interface of Al with its native oxide is the dominant path for diffusion of Cu in single-crystal, and hence also bamboo, Al interconnects.

Using the geometry of the interconnects, the effective diffusivity can be related to ($\alpha\delta D_i$), where α is the segregation coefficient for the Al/AlO_x interface, δ is the width of the interfacial path, and D_i is the interfacial diffusivity. Ignoring any contribution from the lattice or dislocations, and assuming that the sidewalls have the same diffusivity as the top and bottom interfaces, $\alpha\delta D_i$ = 1.2 x 10^{-14} x exp(-0.8 eV/ kT) m^3/s. α has been found to be characterized by a segregational free energy of about 0.2 eV in Al(Cu) thin films [Cop 96].

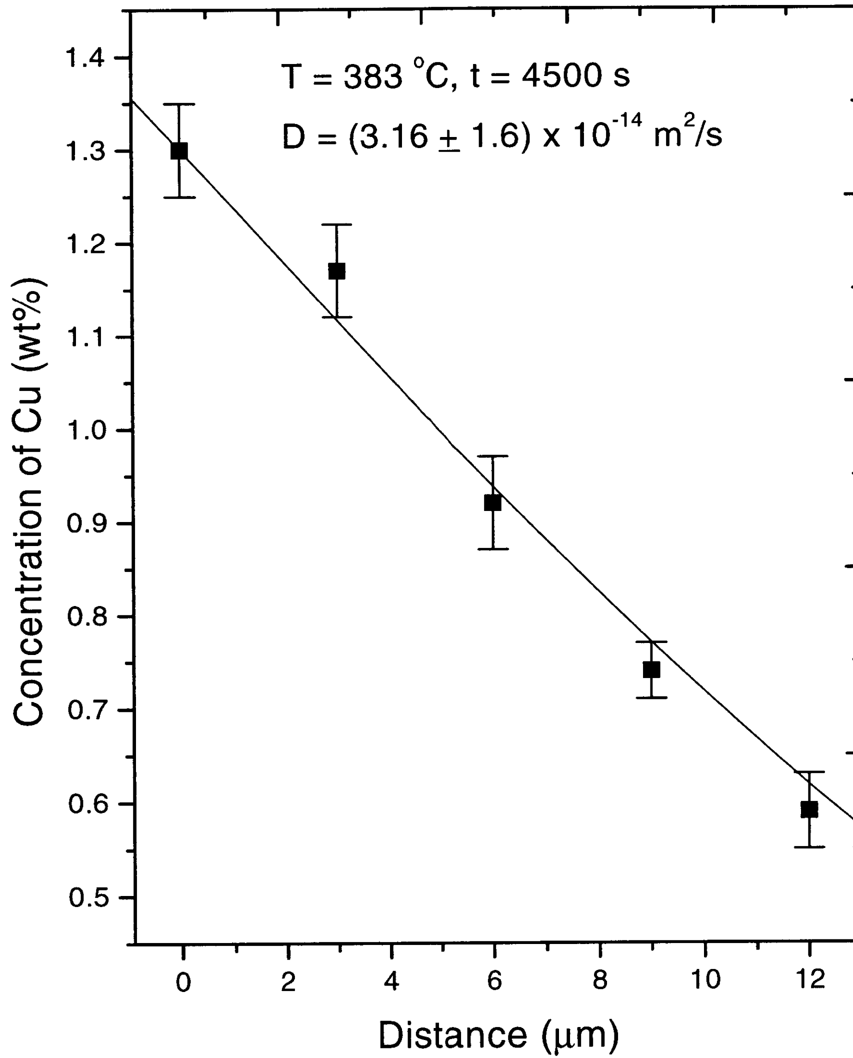

Figure 3-3: Calculation of the diffusivity by nonlinear regression analysis of Equation(3.4).

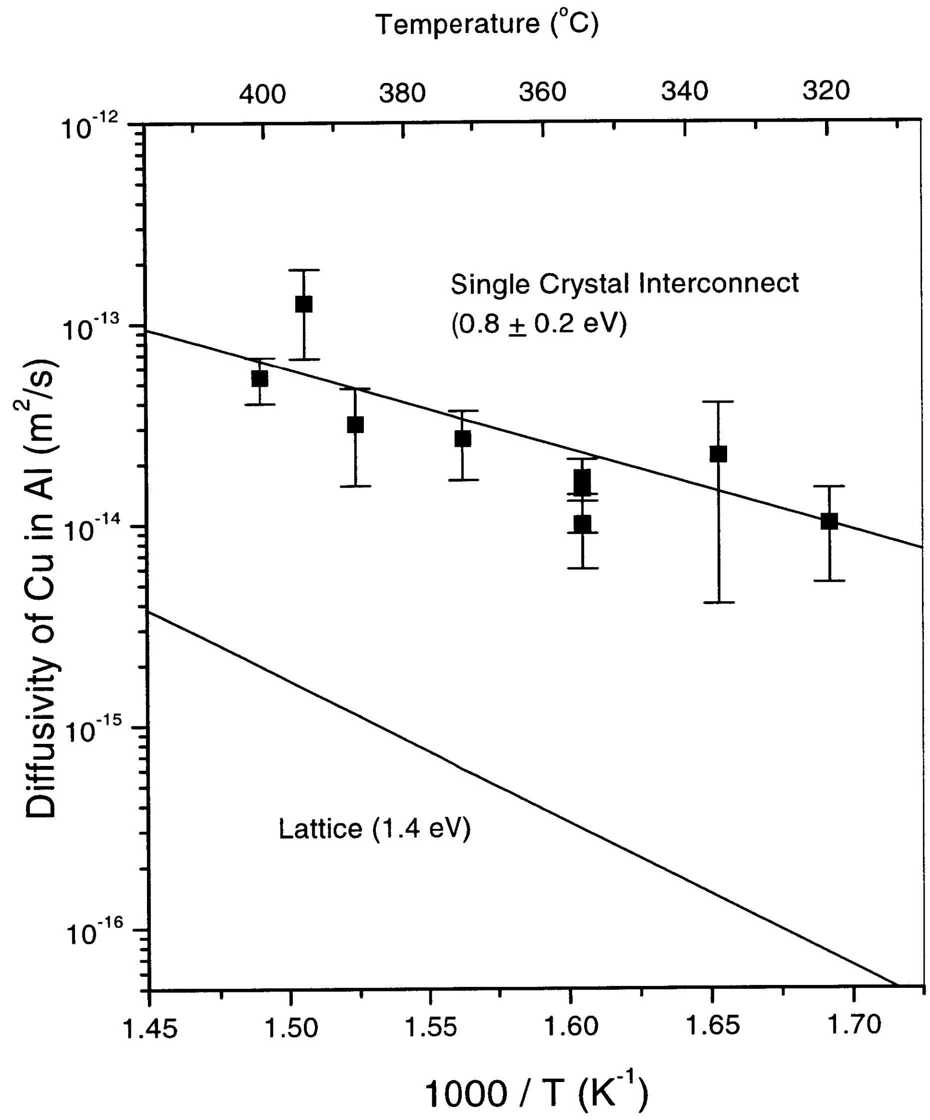

Figure 3-4: Activation energy for diffusion of Cu in single-crystal Al interconnects. Shown for comparison is the corresponding value for diffusion of Cu through the Al lattice [Pet 70].

3.5.2 Effect of Surface-to-Volume Ratio

The conclusion that the transport of Cu occurs through the interfaces can, in principle, be confirmed by performing similar experiments on lines of different geometries. According to Equation (1.9), the effective diffusivity depends on the width (w) and the thickness (h) as

$$D \propto (\frac{1}{w} + \frac{1}{h}) \tag{3.6}$$

The process of fabrication of the Al single crystal films limits the thickness in the range 0.3 μm to 0.5 μm. Hence, the only effective variable is the width of the lines. Figure 3-5 shows a plot of (1/w + 1/h) as a function of w for a line that is 0.4 μm thick. The effective diffusivity remains essentially constant for changes of width in the range 5.0 μm to 1.0 μm. To obtain a measurable difference, one would hence have to study submicron lines. Such dimensions are beyond the capability of the available fabrication facilities. In addition, these lines are now smaller than the spot-size of the electron-probe used in EPMA (1.0 μm), and the measurements of Cu concentration will prove difficult to interpret. For both these reasons, such measurements were not undertaken.

3.5.3 Apparent Effective Valence (Z*)

The value of D at 350 ^{o}C can be used to analyze the data from the electromigration tests, conducted for 3600 seconds. Joule heating leads to an increase in temperature of less than 1 ^{o}C at the test conditions, and was ignored in the analysis. The concentration profile for diffusion aided by electromigration was fit to Equation(3.4), and Z* of Cu was determined to be -6.6 $\pm$ 1.1, as shown in Figure 3-6. Each value of the concentration represents the average of six different measurements. A second measurement of Z* at the same temperature and current-density, but for a shorter time (2400 s), yielded a value of -4.2 $\pm$ 1.4 (Figure 3-7).

The value of Z* of Cu in bulk Al has been measured to be approximately zero

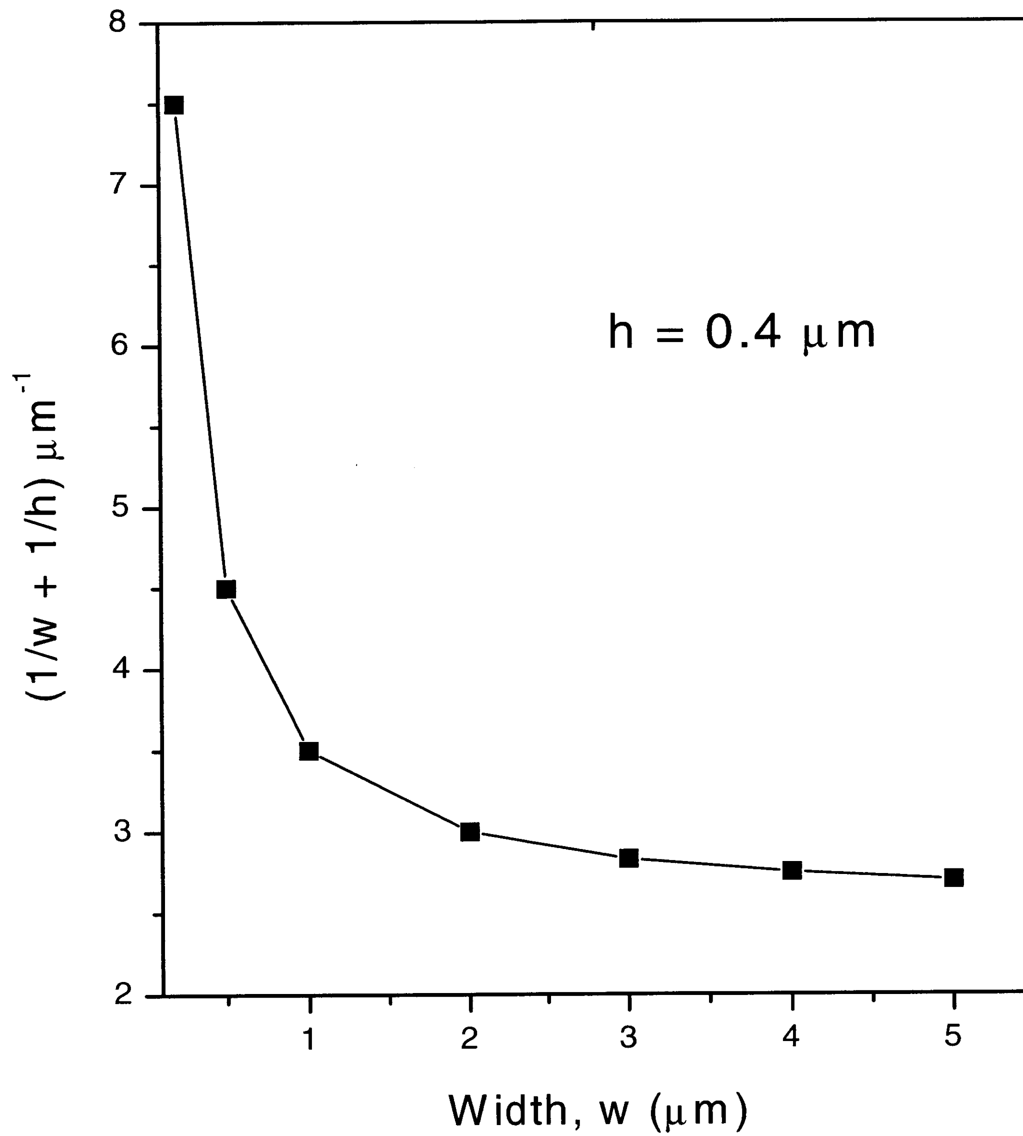

Figure 3-5: The dependence of the effective diffusivity on line width for a 0.4 μm thick single-crystal Al line.

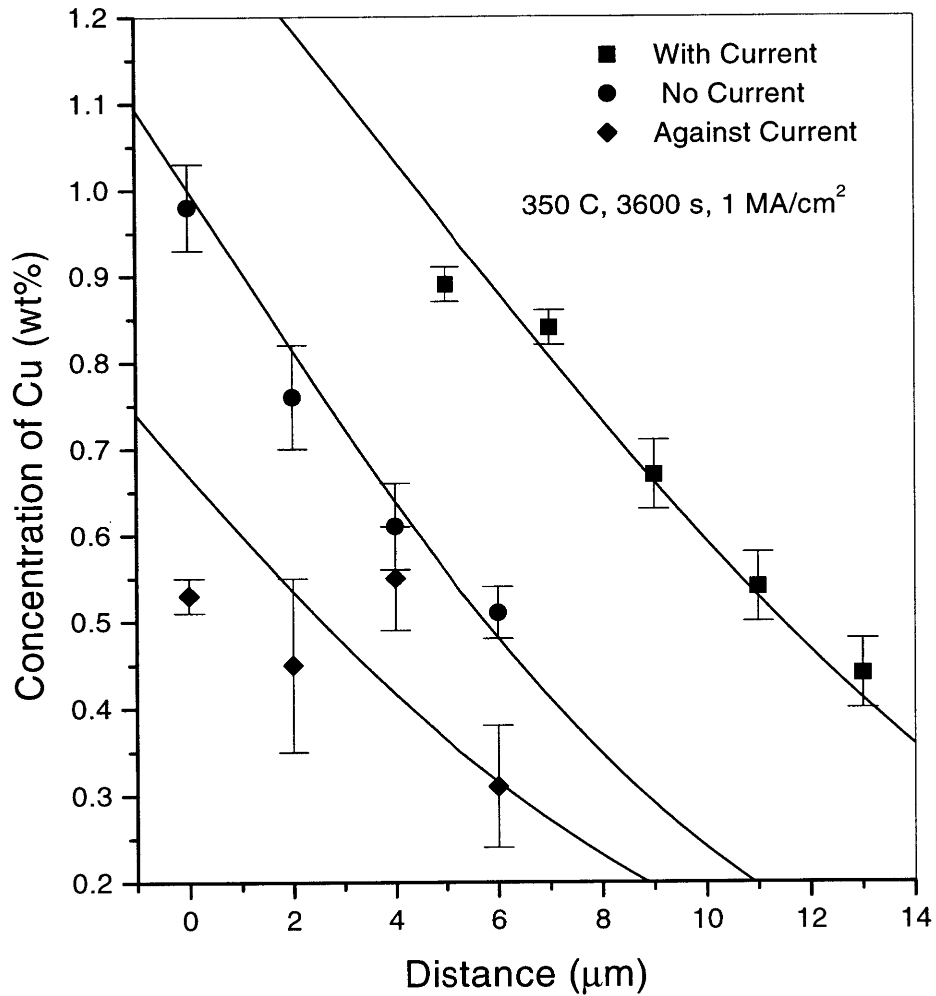

Figure 3-6: Concentration-profile of Cu for diffusion with, without, and against electric current. The test was conducted at 350 °C for 3600 s, using a current-density of 1 MA/cm^2. The solid curves are fits to Equation(3.4) as explained in the text.

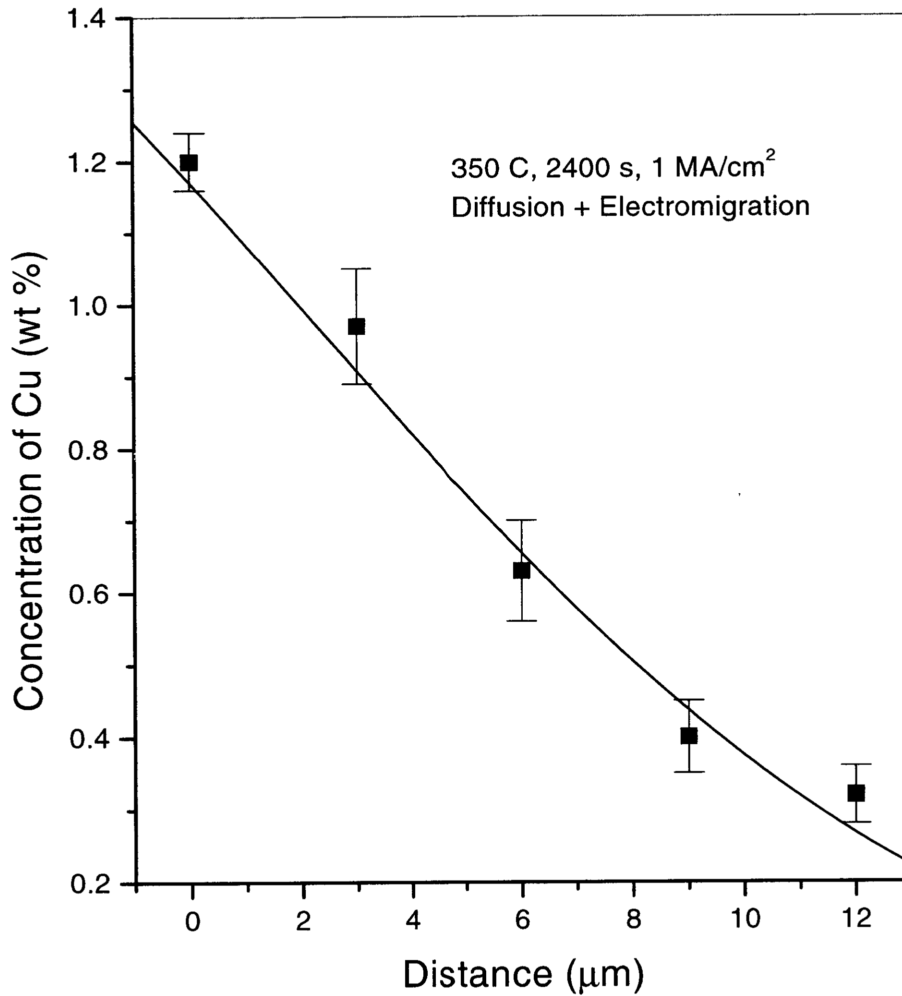

Figure 3-7: Concentration-profile of Cu for diffusion aided by electric current. The test was conducted at 350 ^{o}C for 2400 s, using a current-density of 1 MA/cm^2. The solid curve is a fit to Equation(3.4).

in the range 567 °C to 650 °C [Lim 73], and -16.8 along Al grain boundaries in thin films at 255 °C [Ho 74]. Blech found that Z* of Cu along Al grain boundaries varied between -4.1 and -14.9 in the range 325 °C to 500 °C, and that it was a weak function of temperature and current-density [Ble 77]. By comparison, it appears that the apparent effective valence has similar values for electromigration along the Al/AlO_x interfaces in Al thin films.

The measurements for diffusion opposed by drift had a much lower signal-to-noise ratio as a result of the extremely sharp concentration gradient, as well as the low values of the concentration. No quantitative analysis was attempted on this data, but using the previously determined value of D and Z*, Equation (3.4) captures the trend of the data, as shown in Figure 3-6.

The measurements for the lines not subject to electric field in these tests yielded best-fit values for the effective diffusivity of (1.0 ± 0.5) x 10^{-14} m^2/s, and (1.7 ± 0.4) x 10^{-14} m^2/s, compared to (1.5 ± 0.5) x 10^{-14} m^2/s from the previous diffusion experiment at the same temperature. This is reassuring since the times of test for these experiments were different (3600 s, 2400 s, and 9000 s respectively).

3.5.4 Comparison with Literature

Electromigration experiments on bamboo and near-bamboo Al(Cu) interconnects have indicated that Cu diffuses along the Al/AlO_x and Al/Al_3Ti interfaces [Hu 95a]. Shaw *et al.* measured the rate of dissolution of Al_2Cu precipitates during an *in situ* TEM experiment, and estimated the effective diffusivity of Cu [Sha 96]. The test structure consisted of 0.25 μm thick, 0.5 μm wide Al(Cu) lines (unlayered and unpassivated), and was stressed at 260 °C using a current-density of 0.24 MA/cm^2. Using a value of -5 for Z*, their experiments yield a value for the effective diffusivity at 260 °C in the range 2.9 x 10^{-15} m^2/s to 4.2 x 10^{-15} m^2/s. From the present measurements, the extrapolated value of the effective diffusivity at 260 °C is 3.9 x 10^{-15} m^2/s, in good agreement with their results.

Further, in analogy with the transport of Al, it is expected that the diffusivity of Cu is a weak function of the crystallography of the Al single-crystal [Joo 98].

3.6 Conclusions

The values of the diffusivity and effective valence of Cu in single-crystal Al interconnects have been measured. By a process of elimination, it is concluded that the path for transport of Cu is along the Al/AlO_x interface in these single-crystal lines. These values can be used to simulate electromigration-induced stress evolution in bamboo Al(Cu) interconnects, as described in Chapter 4.

Chapter 4

Numerical Simulation of Electromigration-Induced Stress Evolution in Bamboo Al(Cu) Interconnects

4.1 Background

Electromigration-induced failures in bamboo Al(Cu) interconnects, and the role of Cu in such processes, are not well understood. One study of accelerated lifetime tests on populations of lines showed that the addition of Cu leads to a small increase in lifetime, by a factor of two at most, and that the action of Cu was to strengthen the bamboo grain boundaries [The 97]. These experiments were conducted on unlayered lines, terminating in contact pads. Hu argued that the transport of Al and Cu in bamboo interconnects occurs along the Al/AlO_x and Al/Al_3Ti interfaces, and that Cu inhibits the motion of Al along these interfaces [Hu 95a]. On the other hand, Oates found from drift velocity measurements that the rate and activation energy for drift of Al were consistent with diffusion through the lattice, and that the transport

of Al was unaffected by the presence of Cu [Oat 96, Oat 98]. Formation of Al_2Cu precipitates was found to decrease the lifetimes, depending on the geometry of the conductors [Col 94].

Extrapolation of such data to service conditions is fraught with uncertainty, as noted by Colgan and Rodbell [Col 94]. Typical accelerated tests are conducted at temperatures of 200 - 250 ^oC, and current densities of 2.0 - 2.5 MA/cm^2, while typical service conditions are 75 - 125 ^oC, and 0.2 - 0.5 MA/cm^2. In addition to scaling temperature and current-density, one will also have to account for the variation in the solubility of Cu over the extrapolated temperature range, as well as the variations in the kinetics of precipitation and dissolution. Further, the structures used for accelerated tests may not be representative of the interconnects present in ICs.

A more robust technique for estimating the lifetimes of bamboo Al(Cu) conductors is numerical simulation of electromigration-induced stress evolution at *service* conditions.

4.2 Evolution of the State of Interconnects

In this section, the possible states to which interconnects can evolve are summarized. The interconnects under consideration are bamboo Al(Cu) lines, capped with shunting layers, and embedded in an oxide matrix. The lines terminate in W-studs, which serve to link metal lines present at different levels. The total number of atoms is hence conserved.

Typical processing conditions impose thermal cycles between 450 ^oC and room temperature, generating mechanical stresses due to thermal mismatch between the metal and the surrounding matrix. These stresses can be relaxed either by plastic flow, or by the formation of voids. Hence, prior to the onset of electromigration, interconnects typically have many small voids and some unrelaxed stress.

Application of an electric field leads to electromigration of Al and Cu atoms from

the cathode to the anode. The dynamical behavior of voids under these conditions is extraordinarily complex: they nucleate, annihilate, drift, coalesce, undergo shape change, and break up. However, after a sufficiently long time, the interconnect evolves to a very simple state. A single void remains near the cathode, with all the other voids either getting filled with atoms, or drifting into the cathode void. Redistribution of mass leads to a change in the local stress along the line length. At the cathode, the stress is relaxed in the vicinity of the void. As this void grows, the atoms are deposited in other parts of the line, inducing local stress. This stress gradient opposes electromigration, and at some stage balances it completely. At this point, the interconnect is stable as long as the temperature and current-density are invariant.

The utility of an interconnect in an IC is defined by its resistance. Since the nucleation and growth of voids lead to an increase in resistance by locally forcing the current through the high-resistivity shunts, the size of voids that can be tolerated depends entirely on the maximum tolerable resistance of the line. If the pressure required to stop electromigration is sufficiently large to cause cracking of the oxide, this can lead to extrusion of Al at the anode, leading to a perpetual increase in the resistance (*run away* condition) [Suo 98]. On the other hand, if the oxide does not crack, the resulting stress gradient will define a certain size of void at the cathode, which can be zero if the critical stress for void nucleation is not reached. In such an event, the resistance change reaches a constant value (*saturation resistance*) [Fil 96]. Whether the circuit can tolerate this increase is a purely functional definition.

In the simulation, the intermediate stages of complex void dynamics are ignored. Atoms deplete at the cathode and accumulate at the anode, leading to stress changes. The stress is always assumed to be hydrostatic. Initially, the line is free of voids and has a uniform stress distribution. Application of an electric field leads to electromigration and results in stress evolution as shown in Figure 4-1. When the tensile critical stress is reached at the cathode, a void nucleates and relaxes the stress in its vicinity. It is assumed that the capping layers maintain electrical continuity even after

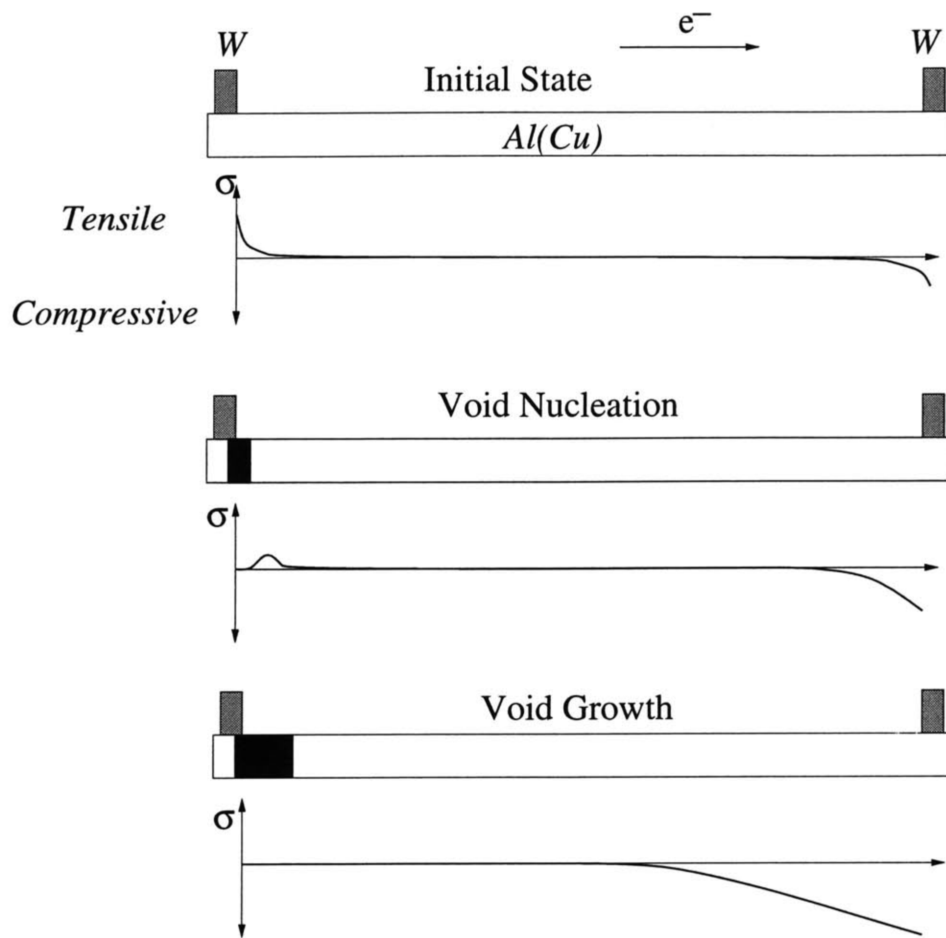

Figure 4-1: Nucleation and growth of voids in a metal line ending in blocking boundaries. The shunting layers on the metal line are not explicitly shown [Par 99].

voiding. With time, the void continues to grow until the driving force for void growth is balanced by the compressive stress at the anode end. At this stage, the maximum void volume is reached, and the resistance stays the same as long as current-density and temperature are invariant.

The change of resistance with time is shown in Figure 4-2. The initial resistance is R, and if the critical stress for nucleation of voids is not reached, the resistance remains R for all time. If the nucleation stress is reached (at time t_n), the void nucleates, and the resistance increases to a maximum value in time t_g as shown.

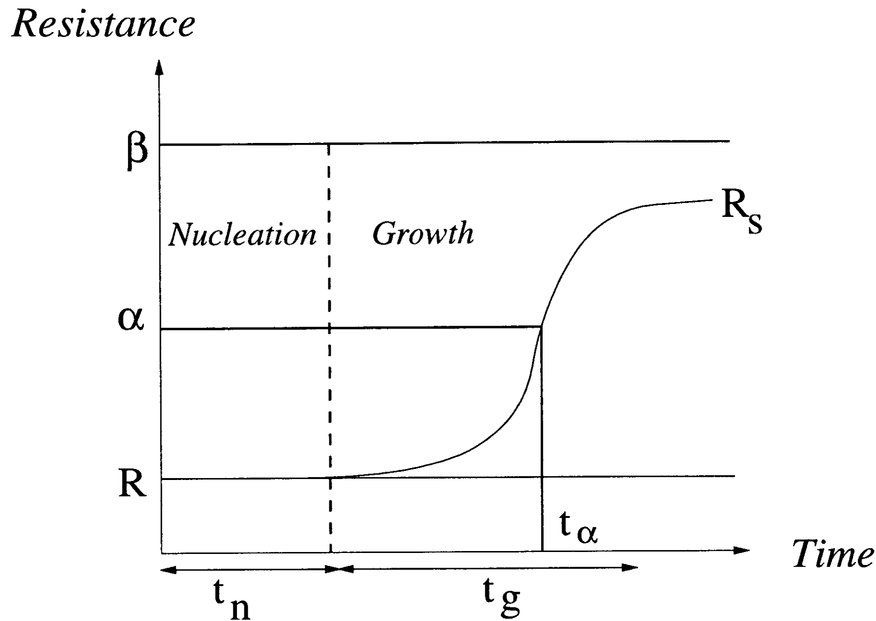

Figure 4-2: Change of resistance with time for a metal line subject to electromigration [Par 99].

Further electromigration will not result in a change in the resistance.

If the system can tolerate a maximum resistance of α, then the interconnect will fail at time t_α. However, if the failure resistance is β, then this interconnect is immortal even though it contains voids. As mentioned before, the value of the resistance at failure is a purely functional definition.

The effects of bamboo grain boundaries are completely ignored. Gleixner and Nix [Gle 98] suggested that unequal distribution of bamboo grain boundaries along the line length could lead to variations in the saturation resistance, since the grain boundaries could act as sinks for atoms. This effect is not accounted for in the simulation. Similarly, the effects of void shape and location are also ignored.

4.3 Details of the Simulation

MIT/EmSim is a program for simulating electromigration-induced stress evolution, and solves Equations (1.6), (1.7), and (1.8), using the forward Euler technique. Variations in microstructure, dependence of diffusivity on stress, alloy additions, and different modes of failure can all be handled by this program, as described in [Par 99]. The results of the simulations described here were obtained using the source code authored by Andleigh [Demo 98].

The spatial and temporal evolution of electromigration-induced stress is simulated by considering incremental volume elements along the line axis (spanning the width of the line), and tracking the atomic flux in and out of these elements. Net changes in the flux are related to changes in stress and vacancy concentration.

The utility of this approach will be illustrated by constructing failure maps for a representative interconnect. Extension to other geometries and trees is straightforward. In addition, the role of Cu in bamboo Al(Cu) lines is investigated using simulations.

4.3.1 Input Values

The necessary input for such simulations was discussed in Chapter 1, and includes the initial state of stress, boundary conditions, physical and materials constants, transport parameters, and test conditions. From the work described in the previous chapters, all these parameters can be estimated.

The most uncertainty exists regarding the diffusivity of Al in such structures. We assume for the purposes of this simulation that this is 100 times larger than the corresponding value through the Al lattice, and that it is unaffected by the presence of Cu.

The thermodynamic interaction between Al and Cu is captured using Murray's

solution model [Mur 85]. The chemical potentials of Al and Cu are represented as

$$\mu^{Al} = \mu_o^{Al} + kTlnX_{Al} + \frac{B - C + 2(3C - B)X_{Al} - (9C - B)X_{Al}^2 + 4CX_{Al}^3}{N}, \quad (4.1)$$

$$\mu^{Cu} = \mu_o^{Cu} + kTlnX_{Cu} + \frac{B - C + 2(3C + B)X_{Cu} - (9C + B)X_{Cu}^2 - 4CX_{Cu}^3}{N}, \quad (4.2)$$

where

$$B = -28353 - 13.5780\,T, \quad (4.3)$$

$$C = 22364 + 12.0517\,T, \quad (4.4)$$

μ_o^{Al} and μ_o^{Cu} are the chemical potentials for pure Al and pure Cu, X_{Al} and X_{Cu} are the mole fractions of Al and Cu respectively, and N is Avogadro's number. This representation assumes that all the Cu is present in solid solution, and ignores the effects of precipitation.

The diffusivity of Cu along the Al/Al_3Ti interface is assumed to be the same as that along the Al/AlO_x interface. The similarity of these diffusivities was shown in Chapter 3 for Al, and it is expected that Cu will follow the same behavior.

First, electromigration failure maps were constructed for a representative interconnect, with systematic variations in current-density and line length. A passivated Al(x at% Cu) interconnect, with bamboo grain structure, ending in W-studs and capped with Al_3Ti shunting layers, was chosen (Figure 4-3). Simulations were conducted for x = 0 and x = 0.2.

The interconnect was assumed to have a square cross-section, with width and thickness equal to 1 μm, and length L. The Al_3Ti shunting layer was assumed to have a total thickness of 0.2 μm, and width of 1 μm. The test temperature was assumed to be 100 ^{o}C.

The resistivity of Al was specified to be 5 $\mu\Omega$cm, and that of Al_3Ti to be 50 $\mu\Omega$cm. The current-density was varied in the range 0.1 to 10 MA/cm^2, and the length was

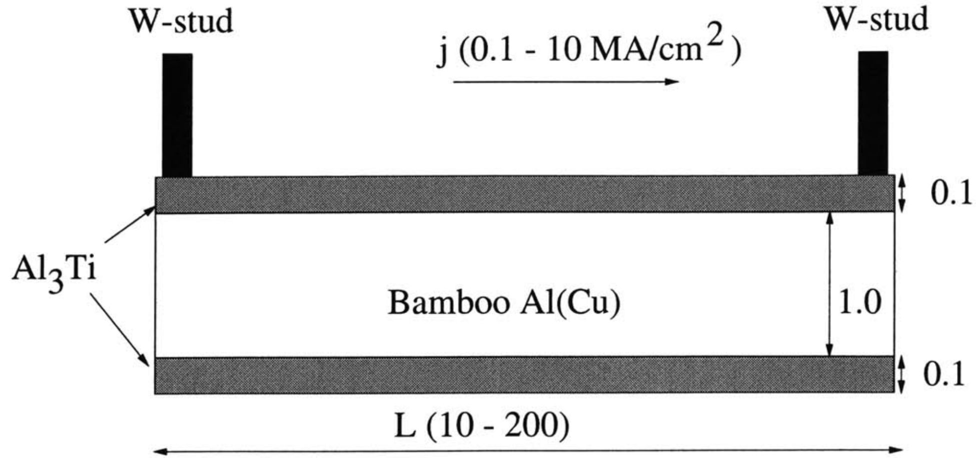

Figure 4-3: Representative interconnect chosen for construction of electromigration failure maps. All dimensions are in μm.

Table 4.1: Physical and Material Constants Used in the Simulations

Boltzmann's constant, k	1.381 x 10^{-23} J K^{-1} 8.617 x 10^{-5} eV K^{-1}
Charge on electron, e	1.602 x 10^{-19} C
Resistivity of Al, ρ_{Al} Resistivity of Al_3Ti, ρ_{Al_3Ti}	5 x 10^{-8} Ωm @ 100 ^{o}C 50 x 10^{-8} Ωm @ 100 ^{o}C
Atomic volume of Al, Ω	1.6 x 10^{-29} m^3/atom
Effective Modulus of Al, B	50 GPa

varied between 10 and 200 μm. The maximum simulation time was 10^6 hours in all cases. The initial stress in the line was assumed to be zero everywhere.

The values of the physical and materials constants used in these simulations are summarized in Table 4.1, and the transport parameters are summarized in Table 4.2.

4.3.2 Definition of Failure

Electromigration-induced stress evolution can lead to the nucleation and growth of voids, and a corresponding increase in the resistance of the line. The critical tensile

Table 4.2: Transport Parameters Used in the Simulations

Parameter	Species	Path	Value
D_{Al}^{Al}	Al	Al lattice	1.6 x 10^{-5} exp(-1.26 eV/kT) m^2/s
$D_{Al}^{AlO_x}$	Al	Al/AlO_x interface	100 x D_{Al}^{Al}
$D_{Al}^{Al_3Ti}$	Al	Al/Al_3Ti interface	100 x D_{Al}^{Al}
$\alpha\delta$ $D_{Cu}^{AlO_x}$	Cu	Al/AlO_x Interface	1.2 x 10^{-14} exp(-0.8 eV/ kT) m^3/s
$\alpha\delta$ $D_{Cu}^{Al_3Ti}$	Cu	Al/Al_3Ti Interface	1.2 x 10^{-14} exp(-0.8 eV/ kT) m^3/s
Z^*_{Al}	Al	Al/AlO_x interface	-2
Z^*_{Al}	Al	Al/Al_3Ti interface	-2
Z^*_{Cu}	Cu	Al/AlO_x interface	-5
Z^*_{Cu}	Cu	Al/Al_3Ti interface	-5

stress for nucleation of voids was specified to be 400 MPa, over and above the initial stress.

Once this stress is reached, voids nucleate and relax the stress in the neighborhood of the cathode as shown in Figure 4-4. It was assumed that the void spans the width and thickness of the line. The initial size of the void can be determined by choosing a length for the stress-relaxation zone (L_{relax} = 0.7 μm), and computing the size of void (L_{void}) as

$$L_{void} = L_{relax} - \frac{(N_{Al} + N_{Cu})\Omega}{wh}, \tag{4.5}$$

where N_{Al} and N_{Cu} are the number of Al and Cu atoms located in the relaxation zone, and w and h are the width and thickness of the line respectively [Par 99].

Depletion of atoms leads to the growth of the void, and to the buildup of compressive stress at the anode, where the atoms accumulate. The critical compressive stress for cracking of the dielectric was chosen to be 800 MPa.

The voiding failure criterion can be based on the change in the resistance of the line, or on the size of the void. Failure maps were constructed for both cases. In the first, failure occurs when the resistance of the line increases by 25%. For lines of length 200 μm and 10 μm, this condition corresponds to void sizes of 1 μm and 0.05 μm respectively. In the second, failure occurs when the void reaches a size of 1 μm,

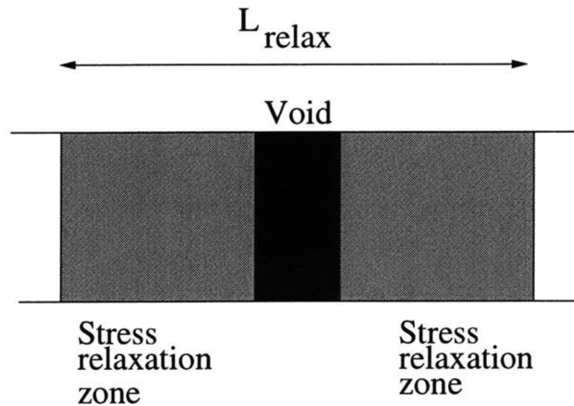

Figure 4-4: Stress-relaxation zone in the vicinity of a void [Par 99].

regardless of the length of the line.

4.3.3 Electromigration Failure Maps

Electromigration failure maps are Cartesian plots with axes of current-density and line-length, showing domains of dominance of various failure mechanisms. They are constructed by computing electromigration-induced stress evolution (using MIT/EmSim), and calculating times to failure using different criteria as explained before. The boundaries between various domains are those combinations of j and L where any two particular mechanisms have the same times to failure.

In general, we can expect the existence of the following domains: an immortal region where the stress for void nucleation is never reached, an effectively immortal region where the resistance saturates below the defined failure value, and domains dominated by void nucleation, void growth, and compressive stress failure. The existence, ordering, and extent of these domains will depend upon the details of the input variables and failure criteria.

4.4 Results

4.4.1 Electromigration Failure Maps for Al(0.2at% Cu)

Two failure maps were constructed based on different definitions of failure. In the first (*R-map*), tensile failure was defined as an increase in resistance by 25% (Figure 4-5). In the second (*V-map*), tensile failure occurred when the void length reached 1 μm, regardless of the length of the line (Figure 4-6).

Both maps show five distinct domains: an immortal region where the critical stress for nucleation is not reached, an effectively immortal region where the failure criterion is not satisfied, failure dominated by nucleation, failure dominated by void growth, and compressive stress failure.

It is readily apparent that the choice of failure condition affects the topology of the failure map. In addition, it is also seen that changing the current-density at fixed length (or equivalently, changing the length at fixed current-density) leads to transitions in the mode of failure.

4.4.2 Electromigration Failure Maps for Bamboo Al

Using the same definitions of failure and the same input parameters as before, electromigration failure maps were constructed for pure Al interconnects. Figure 4-7 shows the failure map based on the failure criterion of 25% increase in electrical resistance. A comparison with Figure 4-5 shows that the failure map is identical to the one constructed for bamboo Al-0.2at% Cu. We conclude from this that Cu has no beneficial effect on the electromigration behavior of bamboo Al interconnects.

4.4.3 Role of Cu in Bamboo Al(Cu)

While copper is known to have a dramatic influence on the lifetime of polygranular Al(Cu), the results of the previous section suggest that it has no beneficial effect in

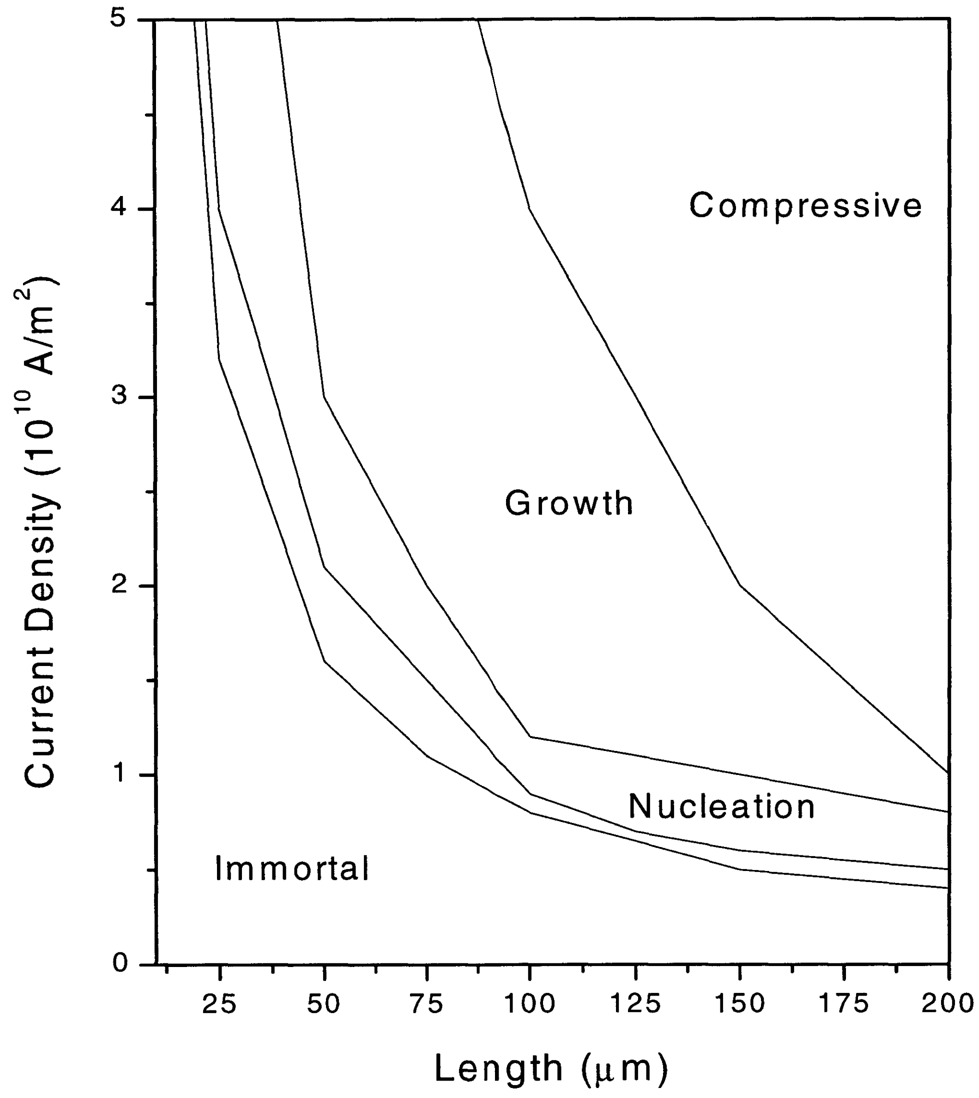

Figure 4-5: Electromigration failure map for bamboo Al(0.2at%Cu) interconnects at 100 °C. Tensile failure corresponds to an increase in resistance by 25%. The unlabeled field corresponds to void saturation.

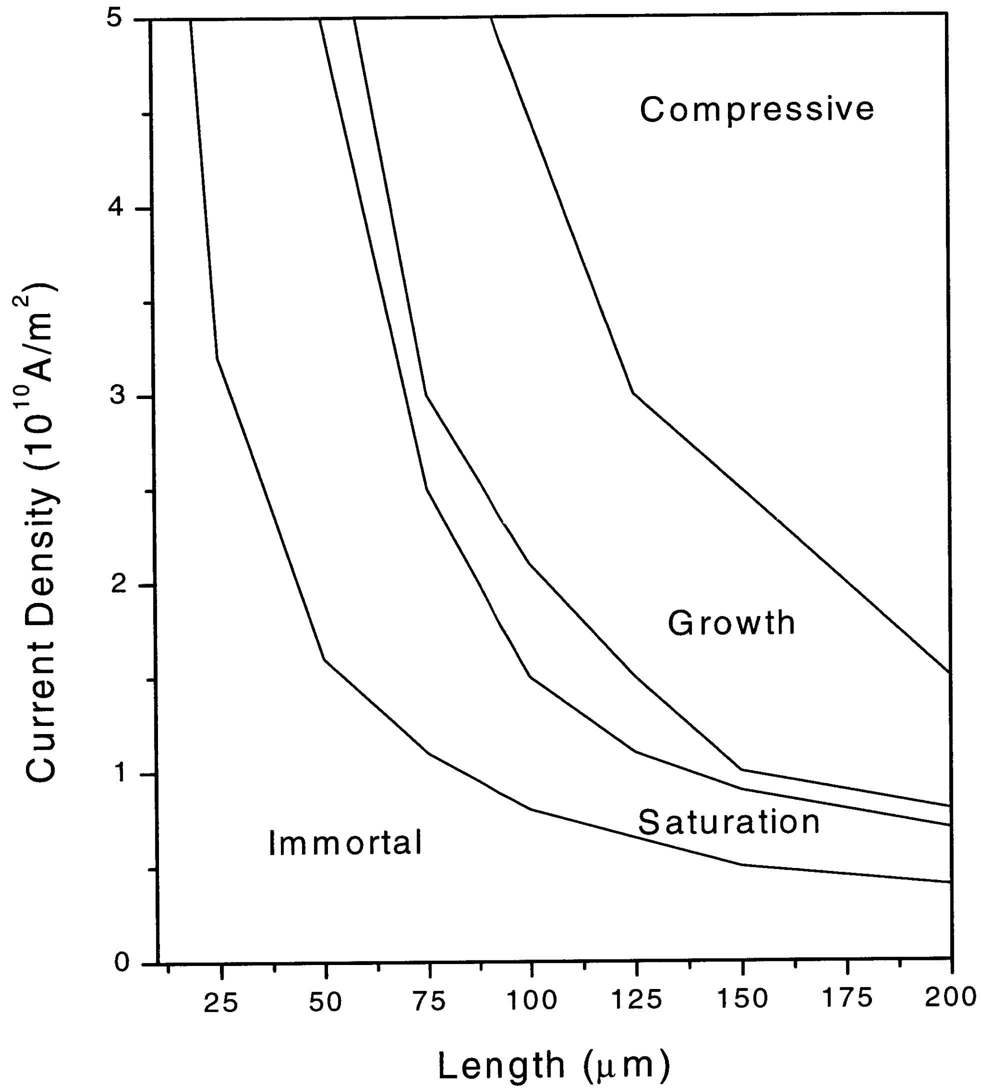

Figure 4-6: Electromigration failure map for bamboo Al(0.2at%Cu) interconnects at 100 ^{o}C. Tensile failure corresponds to a void of length 1 μm. The unlabeled field corresponds to void nucleation-limited failure.

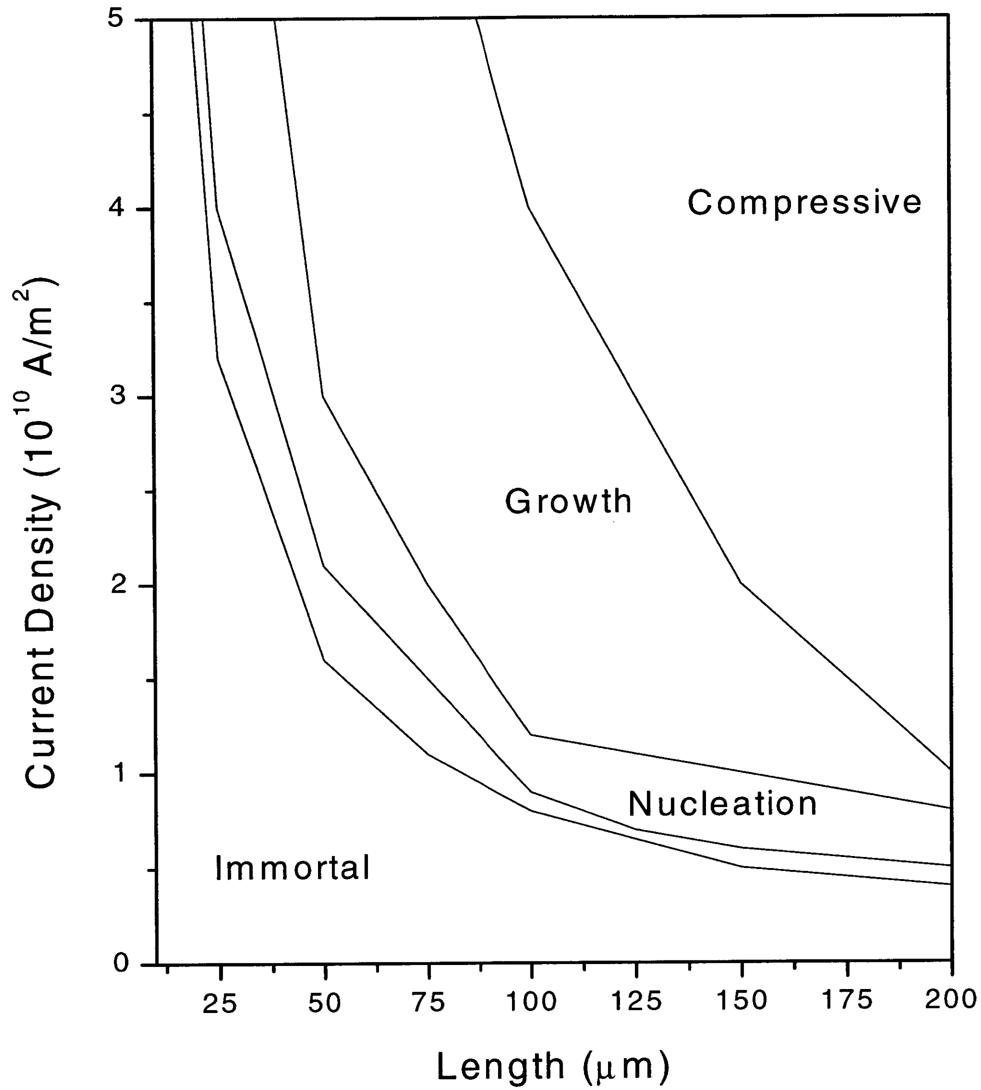

Figure 4-7: Electromigration failure map for bamboo Al interconnects at 100 ^{o}C. Tensile failure corresponds to an increase in resistance by 25%. The unlabeled field corresponds to void saturation.

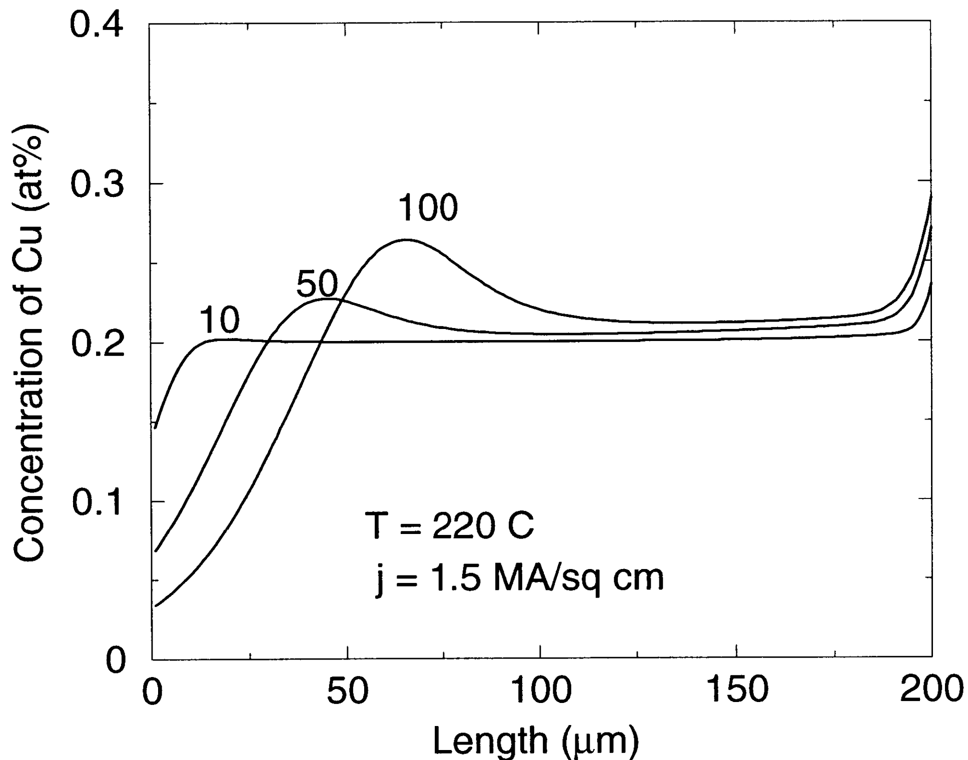

Figure 4-8: Concentration of Cu along a 200 μm long, bamboo Al(Cu) line subject to electromigration. The numbers on top of each curve indicate time in hours.

bamboo Al(Cu). This is not too surprising since it was assumed that Cu does not affect the transport of Al in these simulations.

In order to validate this assumption, the transport of Cu was simulated in a 200 μm long line of square cross-section of side 1 μm, at 220 ^{o}C and 1.5 MA/cm^2. The initial concentration of Cu was set to 0.2 at%, and was assumed to be uniformly distributed along the line length. The line terminated in blocking boundaries.

The diffusivity of Cu at 220 ^{o}C is 4.2 x 10^{-16} m^2/s, found by the extrapolation of the results discussed in Chapter 3. As shown in Figure 4-8, there is substantial removal of Cu away from the cathode, resulting in accumulation of Cu in the rest of the line. The numbers associated with the curves indicate time in hours.

The median times to failure at these conditions in bamboo Al(Cu) lines are greater

than 100 hours [Sri 98]. In times much shorter than this, all the Cu is swept away from the cathode region in bamboo lines. This suggests that the removal of Cu is not the rate limiting process, and hence also that Cu does not play any significant role in improving the electromigration resistance of bamboo Al lines. This conclusion is true at all lower temperatures, since the activation energy for diffusion of Cu (0.8 eV) is less than the activation energy for electromigration failure (1.0 eV).

On the other hand, these simulations ignore the effects of the formation and dissolution of Al_2Cu precipitates. It is possible that increased Cu concentration at the anode can lead to enhanced precipitation, and lower times to failure.

4.5 Discussion

4.5.1 Deviation in the Times to Failure

Electromigration lifetime tests on bamboo Al(Cu) lines reveal significant scatter in the median times to failure. There are at least two possible reasons for this behavior, and neither is captured in these simulations.

The first is the shape, size, and location of the voids. At present, it is assumed that voids nucleate at the cathode end, and span the width of the line. Hence, all the current shunts through the capping layer in this region, leading to a corresponding increase in the resistance of the line. It is obvious that this increase can vary depending on the characteristics of the void.

The second reason is the possible effect of the number and distribution of the bamboo grain boundaries. Gleixner and Nix have argued that bamboo grain boundaries can substantially increase the maximum electromigration stress, based on a two-dimensional finite element calculation [Gle 98]. Consider a line with more boundaries at the anode end compared to the cathode end. As the compressive stress builds up due to accumulation of atoms at the anode, the stress gradient between the edges and the line center drives the atoms into the interior of the grain boundaries, until the

stresses are equalized. Hence, the anode end can accommodate more atoms before the steady-state is reached, since the boundaries now act as atomic sinks. Furthermore, this increase in stress is a function of the distribution of the grain boundaries, and leads to a scatter in the final steady-state stress in bamboo lines.

4.5.2 Initial Stress in Interconnects

The initial state of stress in the lines was assumed to be zero during these simulations. The exact value of the stress prior to electromigration is a function of the details of the thermal cycle. This stress can have profound implications for both the failure and the mode of failure of interconnects. For example, let us consider a bamboo Al(Cu) line terminating in W-studs. At steady-state, a linear stress gradient is established in the line. If the initial stress is zero, and the critical tensile and compressive stresses are as shown in Figure 4-9, then this line is immortal. Now, for the same line, if the initial stress were to be tensile (all other factors remaining constant), it is possible that the steady-state stress will exceed the critical tensile stress, causing the line to fail in tension. A similar analysis can lead the line to fail in compression if the initial stress were to be compressive.

Understandably then, this problem has attracted a lot of attention, and has been addressed experimentally, analytically, and numerically. A first-order model for estimating this stress was presented by Knowlton [Kno 97]. Subsequently, a two-dimensional finite element model capable of calculating stresses as functions of materials, geometry, processing, thermal history, and the details of the plastic and elastic response, was developed [Gou 98]. However, the accuracy of this model depends on the knowledge of the mechanisms of deformation during thermal cycling, and the dependence of the yield stress on geometry. Unfortunately, these remain poorly understood. Appendix C describes some initial experiments to characterize the mechanical behavior of thin Al lines on Si.

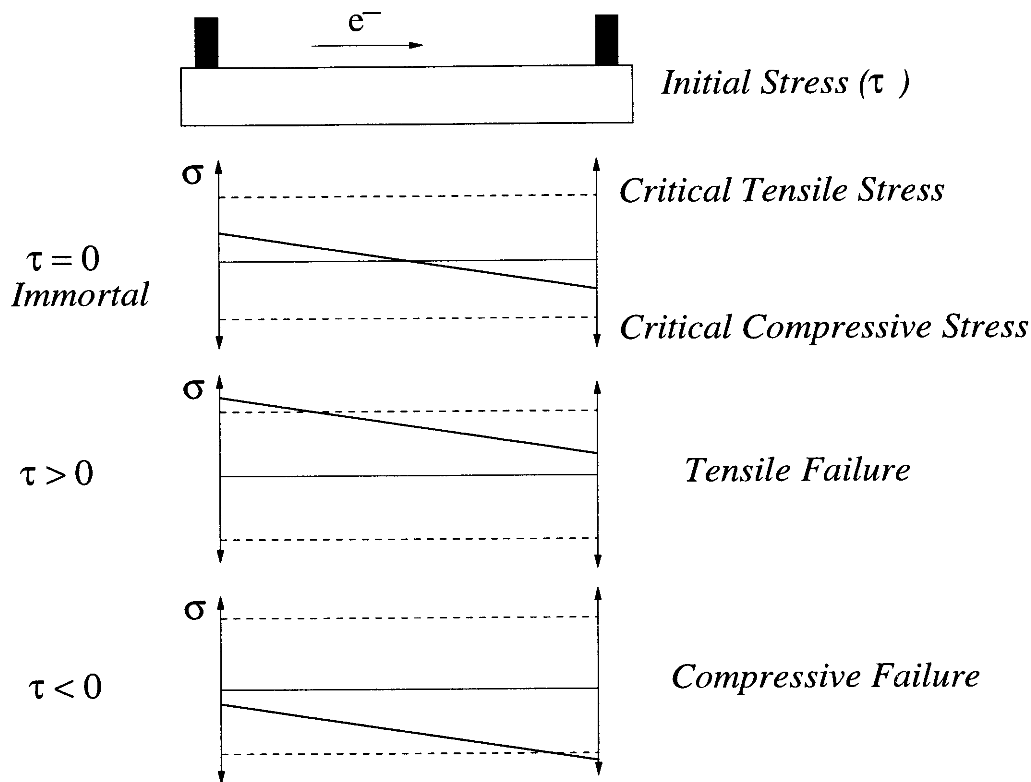

Figure 4-9: Schematic illustration of the effect of initial stress on failure and mode of failure.

4.5.3 Choice of Critical Stresses

The critical stresses for failure are likely to be strong functions of the materials used, the mechanisms involved, and the details of the history of the interconnect. Given this complexity, it is unlikely that the critical values can be estimated from a first-principles calculation.

One approach to estimate these values is to perform accelerated electromigration tests on interconnects of chosen geometry, and to iteratively simulate failure maps to match experimental data [Future].

4.5.4 Utility of Electromigration Failure Maps

Electromigration failure maps provide an overivew of the reliability behavior. They can be readily used to estimate the reliability of interconnects, and to assess the effects of changing current-density and length. They can also lead to a new paradigm for IC design.

The design and fabrication of ICs is a global endeavor of enormous complexity, employing many thousands of people. In recent years, IC sales exceeded $150 billion, and supported an electronics industry with sales approaching $1 trillion!

The current practice is to perform extensive wafer-level electromigration lifetime tests on populations of lines of chosen geometries. These data are then extrapolated to service temperatures, and current-densities, typically using Black's equation (Equation(1.10)), to formulate design rules based on worst-case assumptions. Such rules are usually severely conservative, but in some cases may also be optimistic.

These rules are used to evaluate the reliability of the final circuit. Since ICs contain over a million interconnects, it is not uncommon to expect that some interconnects will not meet these specifications. The circuit will then have to be re-designed at considerable expense.

Hence, the current practice for designing ICs is costly, inflexible, and conservative.

4.5.5 A New Paradigm for IC Design

Ideally, one would like to perform accurate reliability assessment at service conditions, as a functions of the materials used, processing history, geometries, temperature, and current-density. In addition, such assessments should be performed *during* the circuit design phase, and iterated as the circuit undergoes modifications. One approach to this end is an evolving technique based on the use of three computational tools: ERNI, GGSim, and MIT/EmSim [Demo 98].

ERNI is a circuit analysis tool which is used along with a metal layout tool (MAJIC) to subdivide metal levels into interconnect trees. These are the fundamental

units of an IC, and consist of metal lines in electrical contact with each other in a single level. Such trees are binned according to predetermined categories: feature size, current-density, and direction of current for example.

Based on this information, and given the processing conditions used in fabricating these interconnects, GGSim can simulate the process of grain-growth as a function of materials, stress, boundary mobility, and thermal history. The microstructure at service conditions is used as an input to MIT/EmSim.

MIT/EmSim is a tool to solve Equations (1.6), (1.7) and (1.8), given the initial conditions, boundary conditions and transport parameters. Electromigration-induced stress evolution, and subsequent failure, can now be calculated at service conditions. This information can then be cataloged in failure maps, and subsequently used for accurate estimations of reliability.

Chapter 5

Summary and Future Work

5.1 Summary of Results

Electromigration-induced failure remains a serious reliability concern in metal interconnects present in modern integrated circuits. Electromigration in encapsulated metal and alloy interconnects can be modeled using a diffusion-drift equation in one dimension. Solution of this equation leads to the description of the spatial and temporal evolution of the stress along the interconnect. Defining critical values of the stress for various failure modes enables the construction of electromigration failure maps.

Building upon past research, this thesis accomplished this goal for one class of interconnects: Al(Cu) lines with bamboo grain structure, capped with Al_3Ti layers, and terminating in W-studs. Such structures have become increasingly common as interconnect feature sizes shrink with increasing miniaturization.

It has been shown that:

(i) the transgranular transport of Al and Cu occur along the interfaces of the metal and its surrounding matrix. In particular, replacing the Al/AlO_x interface with Al/Al_3Ti resulted in no detectable change in electromigration kinetics and failure mechanisms.

(ii) electromigration-induced stress evolution can be simulated in Al and Al-0.2at% Cu lines with bamboo grain structures, and that electromigration failure maps can be constructed at service conditions. In particular, Cu does not significantly alter the reliability of bamboo Al(Cu) lines.

5.2 Implications of the Results

It has been demonstrated that Cu has no beneficial effect on the electromigration reliability of bamboo Al(Cu) interconnects. Hence using pure Al for the metal levels with narrow lines is suggested. This will have several advantages including a decrease in electrical resistivity (from 3.2 to 2.7 $\mu\Omega$ cm), and ease of fabrication.

5.2.1 Cu-based Metallization

With succeeding generations of ICs, the introduction of new materials and processing techniques is inevitable. The combination of Al(Cu) interconnects (formed by subtractive etching) and SiO_2 passivation has been popular for the past three decades. There is increasing interest in using Cu interconnects and low-k dielectrics at present [Copper]. Introduction of Cu-based metallization will involve re-tooling on a massive scale at enormous expense and the development of new processing techniques. Let us briefly examine the motives for this transition.

At room temperature, Cu has a much lower resistivity (1.7 $\mu\Omega$ cm) compared to Al (2.7 $\mu\Omega$ cm), leading to the possibility of faster operation. In addition, its melting point is almost twice that of Al. One would hence expect Cu lines to operate at lower temperatures and undergo less electromigration than Al at similar operating conditions.

Initial experimental results, however, suggest that the median times to failure of Cu lines under accelerated tests are only an order of magnitude higher than those of bamboo Al lines. Moreover, the activation energy for electromigration-induced failure

in Cu interconnects is about 0.8 eV, compared to 1.0 eV in bamboo Al [Copper]. This, in turn, means that the projected lifetimes at service are about the same for both metals. These results have been interpreted as indications that the transport of Cu occurs along the surfaces and interfaces. It has also been found that alloying Cu with 1%Sn increases the activation energy to 1.3 eV.

However, alloying Cu leads to an increase in the electrical resistivity. For dilute concentrations, most solutes raise the resistivity of Cu by more than 1 $\mu\Omega$ cm per at%. Let us compare Cu and Al lines (of square cross-section), where the Cu is covered with Ta on three sides, and the Al is covered with Al_3Ti on two sides. Figure 5-1 shows the change in the effective resistivity as a function of line width at room temperature. (The temperature coefficient of resistivity is about 0.4%/ ^{o}C for both metals).

The same plot shows the changes in the effective resistivity when the thickness of the barrier layer is increased, suggesting that the improvement in electrical resistivity strongly depends on the composition and geometry of the interconnects. We conclude that the advantage of using Cu over Al has yet to be unequivocally demonstrated. Construction of failure maps at service conditions, based on experimentally determined transport parameters, is a robust technique for making such comparisons.

5.3 Future Work

Following the discussion in Section 1.7, accurate simulation of electromigration in Cu and Cu-alloy interconnects will require knowledge of the transport properties and the initial state of stress.

The transport properties can be obtained by performing experiments analogous to the ones described in Chapters 2 and 3. The evolution of grain structure and stress in Cu films and lines is known to be quite different from that of Al. The mechanical properties of Cu interconnects can be characterized through experiments of the sort described in Appendix C, enabling the estimation of the initial stress. As

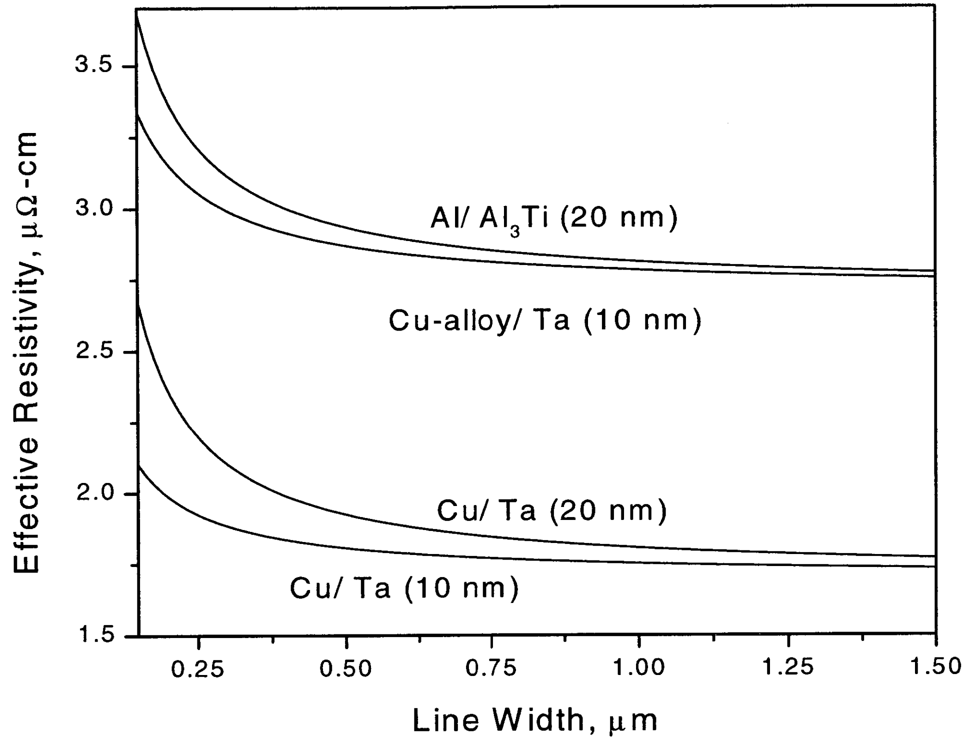

Figure 5-1: Effective resistivity of Al, Cu, and Cu-alloy lines as a function of line width. The lines are assumed to have a square cross-section.

demonstrated in Chapter 4, these values can be used to create failure maps for Cu at service conditions using MIT/EmSim. But, that is quite another story.

Appendix A

Fabrication of Single-Crystal Electromigration Test Structures

The procedures followed to fabricate the Al single crystal test structures are summarized here. More details may be found in Appendix A of Joo's Ph.D. thesis [Joo 95]. Deposition, photo-lithography, and plasma etching were performed in the Building 13 MicroLab at MIT.

A.1 Epitaxial Al Deposition on NaCl Substrates

Epitaxial Al films can be grown on suitable NaCl substrates. Single crystal blocks of NaCl (25 mm x 50 mm x 7 mm) were obtained from Optovac Inc. The orientation of the top flat surface was (110). These blocks were cleaved along the (100) planes into eight pieces, and heated to 200 ^{o}C to remove any absorbed moisture. The top (110) face of each NaCl crystal was then subject to dry and wet polish in order to obtain a smooth and flat surface for epitaxial growth of Al. The dry polish was performed with 4/0 emery paper, and the substrates were sequentially cleaned with (1,1,1)-tricholoroethane, acetone and ethanol for 10 minutes each, using ultrasonic agitation. The wet polish was done using a South Bay Crystal Polisher (Model 451), using a

100:1 mixture of ethanol and water. Typical polishing times were on the order of 1 to 2 minutes. The polished surface was lustrous and free of scratches and grinding pits. These substrates were mounted onto a hot-stage in a CVC thermal evaporator, and eight clips of Al (99.999% pure, 30 mil thick, and 0.75 inches long) were placed on the W filament. The chamber was pumped down to a base pressure of 2 x 10^{-6} torr, and the substrates heated to 320 ^oC at a rate of 5 ^oC/minute. Evaporation was carried out for exactly 10 s, and the samples were allowed to cool down to room temperature inside the chamber.

A.2 Transfer onto Oxidized Si Wafer and Adhesion Anneal

The Al film was detached by dissolving the NaCl in DI water. To ensure that no NaCl remained on the Al film, the film was transfered onto another dish containing clean DI water, and the process repeated three times. Extensive chemical analysis of the final fabricated structures revealed no traces of Na or Cl, indicating that the cleaning procedures were adequate. The floating Al film was then scooped up with a clean oxidized Si wafer. The thickness of the SiO_2 was 1000 $\AA$, and was present in order to prevent the interaction of Al and Si. The scooping process invariably left some water trapped between the Al and the substrate, and this was removed by dragging a wet, clean-room quality, paper towel over the Al film. To ensure a good chemical bond between the Al film and the substrate, the samples were annealed in a vacuum of 10^{-7} torr at 575 ^oC for 1 hour. The Al reduces SiO_2 to form AlO_x during the anneal. Transmission electron microscopy of the sample cross-section confirmed the formation of a 50 $\AA$ thick, continuous AlO_x layer. In addition, the same study found that the Al/AlO_x interface had a wavelength of about 10 $\AA$ [Min 97].

A.3 Patterning, Etching and Passivation

Conventional microfabrication techniques were used on the annealed samples. Shipley 1813 photo-resist was applied using a spin speed of 4300 rpm for 30 seconds. The wafers were cured for 30 minutes at 90 ^oC, and then exposed using a Karl Suss Standard Aligner with 365 nm wavelength UV light. Typical exposure times were 8 to 15 seconds. The exposed wafers were then developed using a solution of Shipley 351 for 1 minute. Finally, the wafers were baked for 30 minutes at 125 ^oC.

Etching and passivation were both done on a Plasma Therm PECVD/ RIE 710 System. The recipes used for etching of Al (with and without Al_3Ti capping layers), deposition of Plasma-Enhanced-Chemical-Vapor-Deposition (PECVD) SiO_2, and etching of SiO_2 are summarized in Tables [A.1], [A.2], and [A.3].

Reactive ion etching of Al was performed using $SiCl_4$ and Cl_2. The base pressure before operation in this system was less than 2 x 10^{-5} torr. The first step was to remove the native AlO_x. This was followed by removal of Al till the patterns could be clearly seen. The etch rate was typically 600 - 700 $\AA$/minute. Sharp side walls were obtained by over-etching during the third step. To avoid corrosion of Al due to any residual Cl_2 in the system, a final passivation step was performed using a mixture of CF_4 and O_2 gases. The photoresist was stripped using an oxygen plasma ash for 5 minutes, using a power of 100 watts and a pressure of 100 mtorr.

PECVD SiO_2 was used to passivate the samples. The deposition rate was of the order of 350 $\AA$/minute and the etch rate in a 7:1 BOE solution was 250 $\AA$/min. The resulting oxide layer was very conformal.

After patterning for contact cuts in the test structure, the oxide was etched using the conditions listed in Table [A.3]. The etch rate of the oxide was about 250 $\AA$/minute. The amount of O_2 in the etching gas was kept low to avoid etching the photoresist.

Table A.1: Parameters for etching Al

Step	Gas (Flow rate)	Pressure	Power/Voltage	Time
I. Breakthrough	$SiCl_4$(30 sccm), Cl_2 (1.5 sccm)	20 mTorr	350 V	30 sec.
II. Bulk etch	$SiCl_4$(30 sccm), Cl_2 (1.5 sccm)	20 mTorr	200 V	Until clear substrate
III. Over etch	$SiCl_4$(30 sccm)	20 mTorr	200 V	20% of Step II
IV. Passivation	CF_4 (40 sccm), O_2 (10 sccm)	100mTorr	50 W	2 min.

Table A.2: Parameters for depositing PECVD SiO_2

Gas (Flow rate)	Pressure	Power	Temperature
SiH_4 + 98%N_2 (400 sccm), N_2O (900 sccm)	900 mTorr	25 W	350° C

Table A.3: Parameters for etching PECVD SiO_2

Gas (Flow rate)	Pressure	Voltage	Time
CF_4 (32 sccm), O_2 (2 sccm)	45 mTorr	300 V	$>$ 10 min.

Appendix B

Dislocation Model for Slit-like Voids

B.1 Introduction

Electromigration-induced voiding in Al-alloy interconnects with polygranular microstructure typically occurs as large, wedge-shaped erosion voids (E-voids). These nucleate and grow at sites of mass flux divergence, such as grain boundary triple points. As the line widths decrease, however, and the microstructure changes from polygranular to bamboo, a second type of void morphology, slit-like voids (S-voids), is also seen [San 92, Ros 92]. While the E-voids cause a local increase in the current-density, the S-voids can grow rapidly to cause open-circuit failure in the absence of current-shunting refractory layers.

Electromigration-induced voiding has been observed in experiments carried out in scanning electron microscopes [Mar 95, Kra 97, Joo 98]. In a typical sequence, an E-void nucleates at the edge of the interconnect, grows, and translates against the flow of electrons. Such voids have been observed to cross grain boundaries, and their shapes can fluctuate as they move from one grain into another. However, a sudden and dramatic change is seen when slit-like voids form. The time for the development of

the slit is usually a small fraction of the time for the entire sequence. The faces of the S-voids are usually planes of the {111} family. Slit-like voids form inside grains (and not at grain boundaries), and have been sometimes observed to form in single-crystal interconnects. This mode of voiding appears to be *triggered* by unknown conditions, and is not the inevitable result of a known specific set of conditions.

Rose analyzed Al-2wt%Cu interconnects by transmission electron microscopy after they had been tested to electromigration failure, and observed that S-voids formed predominantly in non-(111) grains [Ros 92]. Joo and Thompson characterized the dependence of lifetime, as well as void morphology, on crystallographic orientation in Al single-crystal lines with [111] and [110] directions normal to the substrate (alternatively referred to as (111) and (110) textures). The median time to failure of lines with (111)-textures was found to be at least ten times that of lines with (110)-textures. However, there was no dependence, within error limits, on the in-plane orientation of the lines [Joo 97]. In later work on similar single-crystal lines pre-damaged by nanoindentation, it was concluded that neither differences in diffusivity, nor times to nucleation of the voids, could account for these differences in lifetime and void morphologies between the two textures. In addition, it was observed that seemingly identical lines had very different times to formation of S-voids [Joo 98].

B.2 Existing Models

Existing analytical and numerical models explain the S-void to be the result of current-crowding-induced shape instability of E-voids. Among the factors considered have been anisotropic surface energies and diffusivities, the effects of mechanical stress, and finite size effects resulting from the dimensions of the interconnects. Such models have been successful in describing the behavior of E-voids, and some aspects of S-voids. Kraft and Arzt assumed anisotropic surface diffusivities and found that (110)-textured grains were more susceptible to S-voiding than (111)-textured grains,

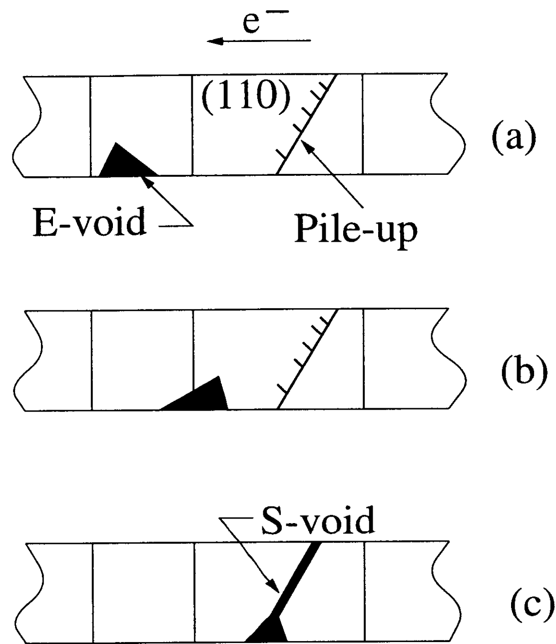

Figure B-1: Schematic illustration of the formation of an S-void by the interaction of a translating E-void with a pileup of dislocations. All the grains are (111)-oriented except for the one marked (110).

and that there was a strong dependence of voiding mode on the in-plane orientation of the lines [Kra 97]. The former is in accord with experimental observations, but the latter is not.

B.3 Role of Dislocation Pile-Ups

It is proposed that stress-relief driven creation of crystallographic defects, and the interaction of such defects with translating E-voids, is fundamentally responsible for the formation of S-voids. In high-stacking fault metals like Al, such defects are probably dislocation pile-ups. This idea is schematically illustrated in Figure B-1. The E-void moves against the direction of electron flow, crosses into a grain of (110) orientation and interacts with the pile-up of dislocations to form the S-void.

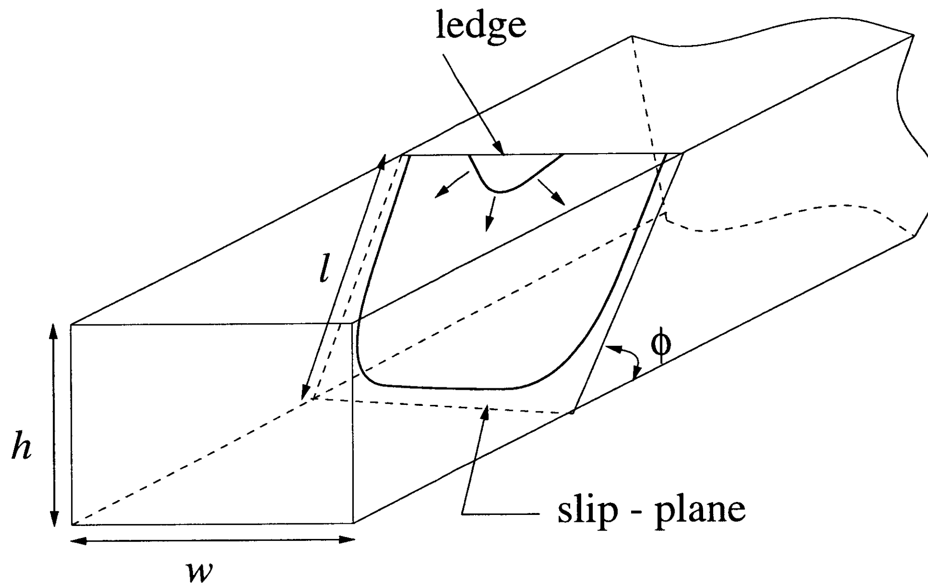

Figure B-2: Schematic illustration of a slip plane in an interconnect containing dislocations.

An upper bound on the stress needed for the operation of such mechanisms is calculated using a model similar in spirit to those employed by Nix [Nix 89], Freund [Fre 87] and Thompson [Tho 93]. The predictions of this model will then be compared to experimental results. Consider a passivated interconnect of thickness h, and width w. The process of transforming a slip plane (of length l) into one of the faces of a S-void can be accomplished in two steps:

(i) Creation of a pileup of n dislocations on this slip plane, and

(ii) replacing this pileup with an S-void with faces of area (lw).

Figure B-2 shows an interconnect with the geometry described above (x, y and z axes are parallel to the length, width and thickness respectively). The dislocations are assumed to originate from the top interface, creating a ledge as they move down the slip plane.

The pileup of n dislocations, each of burgers vector b, can be treated as one

super-dislocation of burgers vector (nb). The work done in creating this pileup is

$$W_\sigma = (\tau nb)(lw), \tag{B.1}$$

where τ is the resolved shear stress on this slip plane.

Following Nix [Nix 89], the energy of the dislocations deposited along the perimeter of the slip-plane is given by

$$W_d = 2(l+w)\frac{(nb)^2}{4\pi(1-\nu)}\frac{2\mu_f\mu_s}{\mu_f+\mu_s}ln(\frac{\beta h}{nb}) = 2(l+w)(nb)^2\epsilon, \tag{B.2}$$

where ν is Poissons ratio, μ is the shear modulus, and the subscripts f and s refer to the film and substrate respectively. It is assumed here that the passivation has similar elastic constants as the Si substrate, and that the energies of the dislocations at the sidewalls and bottom interface are equal to the energy of the ledge at the top interface. β is a constant, approximately equal to unity. The effective elastic constant, ϵ, is about 20 GPa (using μ_{Al} = 24.8 GPa, μ_{Si} = 66.5 GPa, ν = 0.3, b_{Al} = 0.286 nm).

The energy of the faces of the S-void is given by

$$W_s = 2\gamma lw, \tag{B.3}$$

where γ is the surface energy (1 J/m^2 for Al).

The formation of an S-void by the transformation of a dislocation pile-up is energetically feasible if $W_\sigma \geq W_d \geq W_s$. The minimum stress required to operate this mechanism is obtained by equating (B.1), (B.2) and (B.3) in pairs. This leads to two equations which can be solved for the values of n and τ. The critical value of the resolved shear stress is thus

$$\tau = 2\sqrt{\gamma\epsilon}(\frac{l+w}{lw})^{0.5}. \tag{B.4}$$

In general, it is expected that passivated interconnects will be under a triaxial

Table B.1: Critical Resolved Shear Stress (τ)

Texture	$\Sigma 1$	$\Sigma 2$
(110)	$\frac{\sigma}{\sqrt{6}}$	$\frac{2\sigma}{\sqrt{6}}$
(111)	$\frac{2\sigma}{3\sqrt{6}}$	$\frac{7\sigma}{6\sqrt{3}}$

state of stress. In order to capture the entire range of variation, two extreme cases are considered. The first, $\Sigma 1$, corresponds to a weak passivation, such that all components are zero except σ_{xx} and σ_{yy}, with $\sigma_{xx} = \sigma_{yy} = \sigma$. The second case, $\Sigma 2$, corresponds to a 'strong' passivation such that σ_{xx}, σ_{yy}, σ_{zz}, and σ_{yz} are all equal (and equal to σ). Using the analysis of Bishop and Hill [Bis 51], it is possible to calculate the resolved shear stress on each slip system, for an arbitrary stress tensor, as a function of the crystallography of the grain. The highest values of the critical stress for (111) and (110)-textured grains are summarized in Table 1.

B.4 Energetic Feasibility of the Mechanism

For an (110)-textured grain, (with l = w = 1 μm), the maximum stress components for the stress states $\Sigma 1$ and $\Sigma 2$ are 980 MPa and 490 MPa respectively. While stresses of these magnitudes have been measured in interconnects even prior to the onset of electromigration, it is emphasized that these values are an upper bound on the required stress levels. The contribution of the faces of the E-voids has been neglected in this analysis.

The number of dislocations in the pile-up is about 17, and the shear stress required to support such a pileup is about 40 MPa [Wee 71]. The stress at the head of the pileup is about 1 GPa, and can lead to other failure modes, such as cracking of the liners in Cu interconnects.

B.5 Effect of Crystallography

Having concluded that this mechanism is energetically feasible, we can now compare the effect of crystallography: in-plane and out-of-plane orientations. For a grain with (111)-texture (for l = w = 1 μm), the value of σ for $\Sigma 1$ and $\Sigma 2$ are 1470 MPa and 600 MPa respectively. Hence, a significant increase in stress is required before (111)-grains undergo S-voiding, in excellent agreement with experimental observations.

The effect of in-plane orientation can be calculated by allowing the width of the slip plane to vary. For (110)-textured lines, equivalent (111) slip planes are obtained by rotations of 35.25^o or 54.75^o, depending on the sense of rotation. This results in a change in the critical stress by a factor of 1.1, in agreement with the experimental result that there was no measurable effect of in-plane orientation on S-voiding [Joo 95].

B.6 Implications of the Model

The proposed mechanism implies that deterministic modeling of the shape change of E-voids cannot account for S-voids, since the sites of formation of the crystallographic defects are not easily predicted, even with a detailed understanding of the distribution of grains along the length of the interconnect. S-voiding is hence an inherently stochastic phenomenon.

For unlayered lines, this implies that simulations of electromigration as described in the previous chapters will be unable to predict the lifetimes.

B.7 Conclusion

Interaction of stress-relief induced crystallographic defects with translating E-voids to form S-voids has been shown to be an energetically feasible process. The proposed dislocation model is in good agreement with the strong dependence on crystallography, and the inherently stochastic nature, of the S-voids.

Appendix C

Mechanical Behavior of Thin Al Films and Lines on Si

C.1 Background

Stresses in thin films and lines determine the reliability and performance of a large class of technologically important devices. This includes interconnect lines and dielectric layers in microelectronic circuits, and thin films used in magnetic hard disks. Recent reviews of the mechanical behavior of thin films includes [Nix 89, Fro 92].

Interconnect lines can experience significantly high stresses even prior to the onset of electromigration. The origins of these stresses include:
(i) *Intrinsic*: The non-equilibrium processes involved in film formation (nucleation, growth, and coalescence of metal islands for example) can lead to stresses in the film. These can be subsequently modified by grain growth upon exposure to elevated temperatures.
(ii) *Thermal Mismatch*: Interconnects are in intimate contact with a substrate, and may also be encapsulated in a dielectric matrix. The thermal expansion coefficient of all these materials is usually much different from that of the metal itself. Hence, thermal cycling leads to the generation of stresses in the system.

(iii) *Phase Transformation*: In layered interconnects, Al and Ti for example, the reaction to form the Al_3Ti intermetallic phase is associated with a change in the volume of the system, and hence, also with the generation of stresses.

While unpassivated lines are in state of unequal biaxial stress, capped lines experience a state of triaxial stress. One response of the system to relieve this stress is to form voids (*stress voids*). These can lead to failure of the line by themselves, or act as precursors to electromigration failure. In the representation of electromigration as a diffusion-drift equation in stress, as discussed in Chapter 1, a critical stress level is associated with each mode of failure. It is hence of great interest to determine the initial condition of stress in the line as a function of materials, geometry, processing and thermal history. Understandably, this problem has attracted enormous interest in recent years.

Numerical models using the finite element method provide a straightforward procedure for the systematic study of the evolution of thermal stresses and deformation during processing and thermal cycling [Gou 98]. The accuracy of such models depends on the knowledge of the mechanisms of deformation during thermal cycling, and the dependence of the yield stress on geometry. Unfortunately, these remain poorly understood. We seek to study the deformation of thin Al lines of various geometries to characterize the operative mechanisms.

C.2 Experimental Procedures

C.2.1 Sample Fabrication

Four sets of pure Al films of different thickness (0.4, 0.6, 0.8 and 1.0 μm) were sputter-deposited onto oxidized Si substrates. The substrates were 4-inch, (100)-oriented Si wafers, covered with 1000 $\AA$ of thermal SiO_2, and were polished on both sides. The wafers were 460 - 480 μm thick, with a maximum variation of 10 μm. Some films from each set were patterned into gratings of lines covering the entire wafer, using

two different mask sets. The first mask had 1 μm wide lines, separated by 3 μm; while the second mask had 3 μm wide lines, separated by 3 μm.

C.2.2 Wafer-Curvature Measurements

Stress measurements were performed by monitoring the change in curvature of the substrate during thermal cycling (50 - 400 ^oC at 6 ^oC/minute).

The Tencor FLX-2320 system was used to measure the curvatures of wafers. A solid-state laser with 4 mW power, emitting at 620 nm wavelength, is used to scan across the surface of sample while it is heated (or cooled). The temperature can be varied in the range -65 ^oC to 500 ^oC, with ramp rates of up to 10 ^oC/min. The sample is mounted horizontally inside a controlled-atmosphere furnace, with an ambient of air or foaming gas (N_2 -(15%)H_2). The time for each scan is on the order of a second, and real-time measurements as a function of temperature are hence possible.

The use of double-side polished Si wafers was found to be especially useful in the case of the thin lines, since measurements of curvature could be performed on the unprocessed backside. In order to improve the reflectivity, the thermal SiO_2 was removed using plasma etching prior to measurements.

C.3 Deformation in Thin Solid Lines

Kraft and Nix have argued that there are two temperature regimes for the plastic deformation of narrow lines, based on X-ray measurements [Kra 98]. They used arrays of patterned lines (0.72 μm thick) of two different widths: 0.4 μm and 0.8 μm. The lines were covered on the top and bottom by thin Al_3Ti layers, formed by the reaction of Ti with Al. At room temperature, the narrower lines were found to be significantly stronger than the wide lines (which had the same strength as thin films). At higher temperatures, the opposite was observed: a weakening of the narrower lines compared to the wide ones, and was attributed to the operation of diffusional

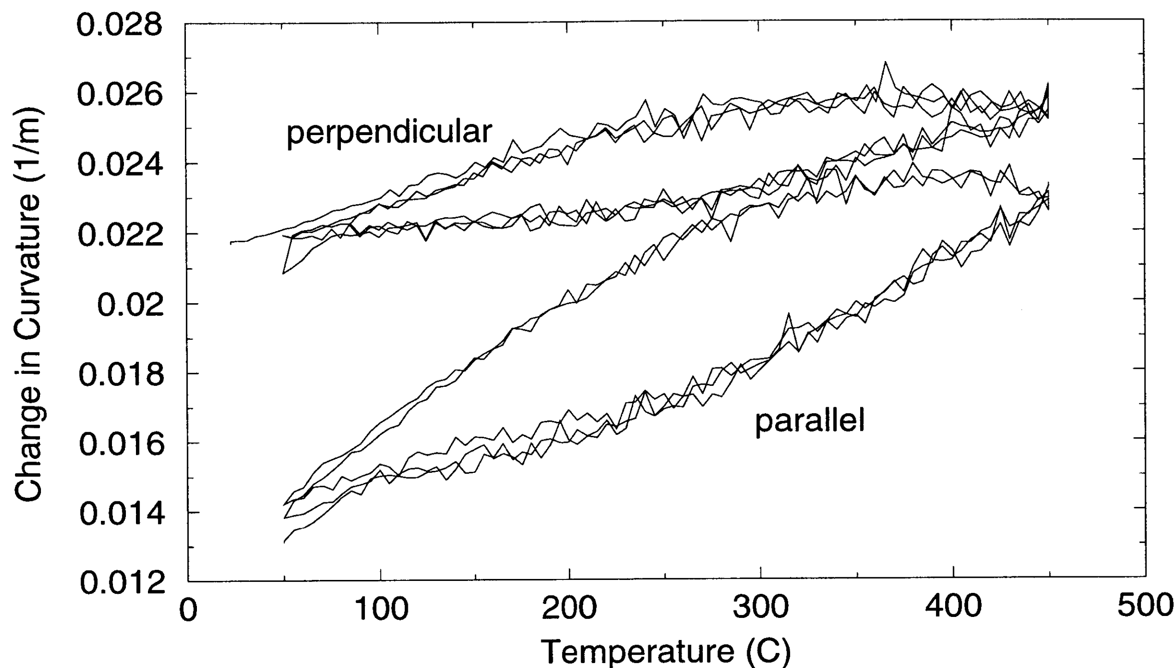

Figure C-1: Curvature - Temperature plot for 3 μm wide, 0.8 μm thick lines.

creep, limited by formation and annihilation of vacancies at the interfaces. Isothermal stress relaxation measurements during the heating cycle indicated a threshold stress of about 40 MPa, below which no relaxation was observed.

In order to further quantify these observations, experiments on a larger variety of line geometries are desirable.

C.4 Results

Figure C-1 shows a typical curvature - temperature plot, in this case for 3 μm wide, 0.8 μm thick lines. Similar curves were obtained for lines of the four different thickness and two different line widths. The response in the direction perpendicular to the lines is much weaker than the response along the lines, as expected. The conversion of these data into stress - temperature plots is in progress [Future].

In addition, isothermal holds were performed at different temperatures in the range 100 - 400 ^{o}C, both during the heating and cooling cycles, for 5.0 hours each. No change in curvature along the line length was detected at any stage (maximum variation in the radius was less than 2 m). This suggests that plasticity is governed mainly by the glide of dislocations, and that creep does not play any role in the deformation of thin lines.

The effect of variations in the ramping rate was investigated for 3 μm wide, 0.8 μm thick lines. The wafers were cycled between 50 ^{o}C and 400 ^{o}C at rates of 0.1, 6.0 and 10.0 ^{o}C/minute. An identical response was obtained in all cases, consistent with the results of the isothermal holds.

Analysis of such data can lead to an understanding of the yield behavior of thin Al lines on oxidized Si substrates.

Bibliography

[Ame 70] I. Ames, F. M. d'Heurle, and R. E. Horstmann. *Reduction of Electromigration in Aluminum Films by Copper Doping*, IBM Journal of Research and Development **14**, 461 (1970).

[Aug 83] S. Augarten. *State of the Art: A Photographic History of the Integrated Circuit*, Ticknor and Fields, New Haven, (1983).

[Ben 92] J. Benedict, R. Anderson, and S. J. Klepeis. *Recent Developments in the Use of the Tripod Polisher for TEM Specimen Preparation*, Materials Research Society Symposium Proceedings **254**, 121 (1992).

[Bis 51] J. F. W. Bishop and R. Hill. *A Theoretical Derivation of the Plastic Properties of a Polycrystalline Face-Centered Metal*, Philosophical Magazine **42**, 1298 (1951).

[Bla 67] J. R. Black. *Mass Transport of Aluminum by Momentum Exchange with Conducting Electrons*, Proceedings of the 6th Annual International Reliability Physics Symposium, 148 (1967).

[Ble 67] I. A. Blech and H. Sello. *The Failure of Thin Aluminum Current-Carrying Strips on Oxidized Silicon*, Physics of Failures in Electronics, **5**, ed. T. S. Shilliday and J. Vaccaro, Rome Air Development Center, 496 (1967).

[Ble 76] I. A. Blech and C. Herring. *Stress Generation by Electromigration*, Applied Physics Letters **29**, 131 (1976).

[Ble 77] I. A. Blech. *Copper Electromigration in Aluminum*, Journal of Applied Physics **48**, 473 (1977).

[Cha 98] N. Chatterjee. *Electron Microprobe Analysis*, 12.141 Course Notes, MIT (1998).

[Cho 89] J. Cho and C. V. Thompson. *Grain Size Dependence of Electromigration-Induced Failures in Narrow Interconnects*, Applied Physics Letters **54**, 2577 (1989).

[Cle 95] J. J. Clement and C. V. Thompson. *Modeling Electromigration-Induced Stress Evolution in Confined Metal Lines*, Journal of Applied Physics **78**, 900 (1995).

[Col 90] E. G. Colgan. *A Review of Thin-Film Aluminide Formation*, Materials Science Reports **5**, 3 (1990).

[Col 94] E. G. Colgan and K. P. Rodbell. *The Role of Cu Distribution and Al_2Cu Precipitation on the Electromigration Reliability of Submicrometer Al(Cu) Lines*, Journal of Applied Physics **75**, 3423 (1994).

[Coo 94] S. Cooperman. *S.M. Thesis*, Massachusetts Institute of Technology (1994).

[Cop 96] M. Copel, K. P. Rodbell, and R. M. Tromp. *Cu Segregation at the Al(Cu)/Al_2O_3 Interface*, Applied Physics Letters **68**, 1625 (1996).

[Copper] J. M. E. Harper, E. G. Colgan, C-K. Hu, J. P. Hummel, L. P. Buchwalter and C. E. Uzoh. *Materials Issues in Copper Interconnections*, MRS Bulletin **XIX**, 23 (1994); R. Rosenberg and C-K. Hu. *Electromigration Characteristics of Copper Interconnects*, SRC/SEMATECH TRC on Reliability (1997).

[Cul 78] B. D. Cullity. *Elements of X-Ray Diffraction* (Second Edition), Addison-Wesley (1978).

[Demo 98] *http://nirvana.mit.edu/darpademo/all3tools.html*

[Fik 59] V. B. Fiks. *On the Mechanism of the Mobility of Ions in Metals*, Soviet Physics Solid State **1**, 14 (1959).

[Fil 96] R. G. Filippi, R. A. Wachnik, H. Aochi, J. R. Lloyd, and M. A. Korhonen. *The Effect of Current Density and Stripe Length on the Resistance Saturation during Electromigration Testing*, Applied Physics Letters **69**, 2350 (1996).

[Fre 87] L. B. Freund. *The Stability of a Dislocation Threading a Strained Layer on a Substrate*, Journal of Applied Mechanics **54**, 553 (1987).

[Fro 92] H. J. Frost. *Deformation Mechanisms in Thin Films*, Materials Research Society Symposium Proceedings **265**, 3 (1992).

[Future] Research groups of C. V. Thompson, D. Troxel, and S. Suresh, MIT.

[Gle 98] R. J. Gleixner and W. D. Nix. *Effect of Bamboo Grain Boundaries on the Maximum Electromigration-Induced Stress in Microelectronic Interconnect Lines*, Journal of Applied Physics **83**, 3595 (1998).

[Gol 92] J. I. Goldstein, D. E. Newbury, P. Echlin, D. C. Joy, A. D. Romig, C. E. Lyman, C. Fiori, and E. Lifshin. *Scanning Electron Microscopy and X-ray Microanalysis: A Text for Biologists, Materials Scientists, and Geologists* (Second Edition), Plenum Press, NY (1992).

[Gou 98] A. Gouldstone, Y-L. Shen, S. Suresh, and C. V. Thompson. *Evolution of Stresses in Passivated and Unpassivated Metal Interconnects*, Journal of Materials Research **13**, 1956 (1998).

[Gup 78] D. Gupta, D. R. Campbell, and P. S. Ho. *Thin Films: Interdiffusion and Reactions*, ed. J. Poate, K. N. Tu, and J. Mayer, Wiley, New York, Chapter 7 (1978).

[Her 50] C. Herring. *Diffusional Viscosity of a Polycrystalline Solid*, Journal of Applied Physics **21**, 437 (1950).

[Ho 74] P. S. Ho and J. K. Howard. *Grain-Boundary Solute Electromigration in Polycrystalline Films*, Journal of Applied Physics **45**, 3229 (1974).

[How 71] J. K. Howard and R. F. Ross. *Hillocks as Structural Markers for Electromigration Rate Measurements in Thin Films*, Applied Physics Letters **18**, 344 (1971).

[Hu 95] C-K. Hu, K. P. Rodbell, T. D. Sullivan, K. Y. Lee, and D. P. Bouldin. *Electromigration and Stress-Induced Voiding in Fine Al and Al-Alloy Thin-Film Lines*, IBM Journal of Research and Development **39**, 465 (1995).

[Hu 95a] C-K. Hu. *Electromigration Failure Mechanisms in Bamboo-Grained Al(Cu) Interconnects*, Thin Solid Films **260**, 124 (1995).

[Hun 61] H. B. Huntington and A. R. Grone. *Current-Induced Marker Motion in Gold Wires*, Journal of Physics and Chemistry of Solids **20**, 76 (1961).

[Joo 95] Y-C. Joo. *Ph.D. Thesis*, Massachusetts Institute of Technology (1995).

[Joo 97] Y-C. Joo and C. V. Thompson. *Electromigration-Induced Transgranular Failure Mechanisms in Single-Crystal Aluminum Interconnects*, Journal of Applied Physics **81**, 6062 (1997).

[Joo 98] Y-C. Joo, S. P. Baker, and E. Arzt. *Electromigration in Single-Crystal Aluminum Lines with Fast Diffusion Paths made by Nanoindentation*, Acta Materialia **46**, 1969 (1998).

[Kno 97] B. D. Knowlton. *Ph.D. Thesis*, Massachusetts Institute of Technology (1997).

[Kor 93] M. A. Korhonen, P. Børgesen, K. N. Tu, and C-Y. Li. *Stress Evolution due to Electromigration in Confined Metal Lines*, Journal of Applied Physics **73**, 3790 (1993).

[Kor 95] M. A. Korhonen, T. Liu, D. D. Brown, and C-Y. Li. *Stress-Voiding and Electromigration in Multilevel Interconnects*, Materials Research Society Symposium Proceedings **391**, 411 (1995).

[Kra 97] O. Kraft and E. Arzt. *Electromigration Mechanisms in Conductor Lines: Void Shape Changes and Slit-Like Failure*, Acta Materialia **45**, 1599 (1997).

[Kra 98] O. Kraft and W. D. Nix. *Thermomechanical Behavior of Continuous and Patterned Al Thin Films*, Materials Research Society Symposium Proceedings **516**, 201 (1998).

[Lim 73] Y. Limoge. *Electromigration of Copper, Silver and Gold in Aluminum*, Solid State Communications **12**, 1141 (1973).

[Llo 96] J. R. Lloyd. *30 Years of Electromigration Research: A Grand Masters' Perspective*, Materials Research Society Symposium Proceedings **428**, 3 (1996).

[Mar 95] T. Marieb, P. Flinn, J. C. Bravman, D. Gardner, and M. C. Madden. *Observations of Electromigration Induced Void Nucleation and Growth in Polycrystalline and Near-Bamboo Passivated Al lines*, Journal of Applied Physics **78**, 1026 (1995).

[Min 97] B. Miner, S. Bill, V. T. Srikar, and C. V. Thompson. Unpublished Research (1997).

[Mur 85] J. L. Murray. *The Aluminum-Copper System*, International Metals Review **30**, 211 (1985).

[Nix 89] W. D. Nix. *Mechanical Properties of Thin Films*, Metallurgical Transactions **20A**, 2217 (1989).

[Oat 96] A. S. Oates. *Electromigration Transport Mechanisms in Al Thin-Film Conductors*, Journal of Applied Physics **79**, 163 (1996).

[Oat 98] A. S. Oates. *Stress Induced Phenomena in Metallization: 4th International Workshop*, 39 (1998).

[Par 99] Y-J. Park, V. Andleigh, and C. V. Thompson. *Simulations of Stress Evolution and the Current-Density Scaling of Electromigration-Induced Failure Times in Pure and Alloyed Interconnects*, Journal of Applied Physics (1999).

[PaP 90] J. L. Pouchou and F. Pichoir. *Surface Film X-Ray Microanalysis*, Scanning **12**, 212 (1990).

[Pet 70] N. L. Peterson and S. J. Rothman. *Impurity Diffusion in Aluminum*, Physical Review B**1**, 3264 (1970).

[Ros 92] J. H. Rose. *Fatal Electromigration Voids in Narrow Aluminum-Copper Interconnect*, Applied Physics Letters **61**, 2170 (1992).

[San 92] J. E. Sanchez, L. T. Mcknelly, and J. W. Morris. *Slit Morphology of Electromigration Induced Open Circuit Failures in Fine Line Conductors*, Journal of Applied Physics **72**, 3201 (1992).

[Sha 96] T. M. Shaw, C-K. Hu, K. Y. Lee, and R. Rosenberg. *Copper Migration and Precipitate Dissolution in Aluminum/Copper Lines during Electromigration Testing*, Materials Research Society Symposium Proceedings **428**, 187 (1996).

[Sri 98] T. S. Sriram. Private Communication (1998).

[Suo 94] Z. Suo. *Electromigration-Induced Dislocation Climb and Multiplication in Conducting Lines*, Acta Metallurgica et Materialia **42**, 3581 (1994).

[Suo 98] Z. Suo. *Stable State of Interconnect under Temperature Change and Electric Current*, Acta Materialia **46**, 3725 (1998).

[Tar 85] J. Tardy and K. N. Tu. *Solute Effect of Cu on Interdiffusion in Al_3Ti Compound Films*, Physical Review B**32**, 2070 (1985).

[The 97] S. Theiss, J. Prybyla, and M. A. Marcus. *The Effect of Cu Concentration and Distribution on the Lifetimes of Submicron Bamboo Al(Cu) Runners*, Materials Research Society Symposium Proceedings **473**, 387 (1997).

[ThL 93] C. V. Thompson and J.R. Lloyd. *Electromigration and IC Interconnects*, MRS Bulletin **XVIII**, 19 (1993).

[Tho 86] C. V. Thompson and J. Cho. *A New Electromigration Testing Technique for Rapid Statistical Evaluation of Interconnect Technology*, IEEE Electron Device Letters **EDL-7**, 667 (1986).

[Tho 93] C. V. Thompson. *The Yield Stress of Polycrystalline Thin Films*, Journal of Materials Research **8**, 237 (1993).

[Vai 80] S. Vaidya, T. T. Sheng, and A. K. Sinha. *Linewidth Dependence of Electromigration in Evaporated Al-Cu*, Applied Physics Letters **36**, 464 (1980).

[Vol 71] T. E. Volin, K. H. Lie, and R. W. Balluffi. *Measurement of Rapid Mass Transport along Individual Dislocations in Aluminum*, Acta Metallurgica **19**, 263 (1971).

[Wal 92] D. T. Walton, H. J. Frost, and C. V. Thompson. *Development of Near-Bamboo and Bamboo Microstructures in Thin-Film Strips*, Applied Physics Letters **61**, 40 (1992).

[Wal 98] R. A. Waldo. *GMRFILM*, MAS Software Library, U. of Michigan, Ann Arbor, MI.

[Wee 71] J. Weertman and J. R. Weertman. *Elementary Dislocation Theory*, The Macmillan Co. London (1971).

[You 82] W. Yourgrau, A. van der Merwe, and G. Raw. *Treatise on Irreversible and Statistical Thermodynamics*, Dover Publications, New York (1982).